Exploring the reliability of DFT calculations of the infrared and terahertz spectra of sodium peroxodisulfate

Supplementary information

John Kendrick
j.kendrick@leeds.ac.uk

Andrew Burnett
a.d.burnett@leeds.ac.uk

October 22, 2019

Contents

List of Tables

List of Figures

1 Crystal Basis Sets

Details of the number of uncontracted Gaussian functions and their contractions are given in Table 1 for the TZVP and the larger DEF2 molecular basis sets used for the Crystal calculations. Both Crystal14 and Crystal17 were used. All results reported in the main text are calculated with Crystal17. Crystal14 was used for the determination of the optimum dispersion parameters in the GD2 calculations.

Table 1: Crystal Basis Sets

Basis	Atom	Number of uncontracted functions	Contraction pattern
TZVP	S	14s,8p,1d	73211,5111,1
TZVP	Na	14s,7p,1d	73211,511,1
TZVP	O	10s,6p,1d	6211,411,1
DEF2	S	14s,9p,3d	73211,51111,21
DEF2	Na	13s,7p,2d	7321,511,11
DEF2	O	11s,6p,2d	62111,411,11

2 Convergence Criteria

2.1 k-point sampling

Convergence in k-point sampling was examined using three Monkhurst-Pack grids in VASP calculations of the PBE optimized unit cell, with an energy cut-off of 560 eV. The results are shown in Table 2, which shows the behaviour of the lattice energy, the calculated unit-cell volume and the frequencies of the two lowest optical modes at the gamma point.

Table 2: K-point sampling

Sampling	No. of k-points	Energy (eV)	Volume ($Å^3$)	Mode 4 (cm^{-1})	Mode 5 (cm^{-1})
7,6,5	106	-67.58701	162.48171	76.23	91.65
8,7,6	170	-67.58703	162.47987	76.11	90.86
9,8,7	253	-67.58701	162.48014	76.22	91.60

2.2 Cut-off Energy

To examine the behaviour with respect to cut-off energy, calculations were performed using the experimental unit cell dimensions, with full optimization of the atomic positions within the symmetry constraints of the space-group. The PBE functional was used with a 7,6,5 Monkhurst-Pack grid. In Table 3 to Table 7 ϵ_{ionic} and ϵ_{elec} are the ionic and electronic contributions respectively to the permittivity at zero frequency. Calculations of the ionic and electronic contributions to the permittivity and the frequencies were performed with the Density Functional Perturbation Theory (DFPT) module of the packages considered. No sum rules were used in the calculation of the phonon frequencies as calculated by the DFT packages. However, the values reported in the tables and the shifts in frequency were calculated from the package output using the PDielec package, with the translational phonon modes projected out. The reference frequencies used to calculated the shifts were the frequencies calculated by the highest energy cut-off.

In the tables the root mean squared shifts (RMSS) in frequency are calculated for all the optical phonon modes at the gamma point. In the case of the Abinit package the root mean squared frequency shifts given in brackets are calculated ignoring the lowest non-zero phonon frequency.

Table 3: Abinit cutoff energy behaviour for FHI pseudo-potentials

Cut-off Energy (eV)	Total Energy (eV)	Pressure (GPa)	$\epsilon_{\mathbf{ionic}}$	$\epsilon_{\mathbf{elec}}$	Frequency RMSS (cm^{-1})
1088.5	-4066.334	1.766	3.814	2.389	5.02 (2.30)
1360.6	-4066.402	1.584	3.181	2.389	3.80 (2.31)
1632.7	-4066.482	1.710	3.205	2.389	4.08 (1.57)
1904.8	-4066.510	1.864	3.206	2.389	2.43 (1.46)
2176.9	-4066.516	1.915	3.271	2.389	

Table 4: Abinit cutoff energy behaviour for ONCVPSP pseudo-potentials

Cut-off Energy (eV)	Total Energy (eV)	Pressure (GPa)	$\epsilon_{\mathbf{ionic}}$	$\epsilon_{\mathbf{elec}}$	Frequency RMSS (cm^{-1})
1088.5	-6698.018	2.181	2.252	2.435	10.42
1360.6	-6698.050	2.683	3.044	2.436	2.43
1632.7	-6698.058	2.674	3.086	2.435	1.86
1904.8	-6698.064	2.677	3.021	2.435	1.65
2176.9	-6698.067	2.687	3.005	2.435	

Table 5: CASTEP cutoff energy behaviour

Cut-off Energy (eV)	Total Energy (eV)	Pressure (GPa)	$\epsilon_{\mathbf{ionic}}$	$\epsilon_{\mathbf{elec}}$	Frequency RMSS (cm^{-1})
1000	-6564.995	-0.942	2.854	2.437	2.19
1300	-6565.178	1.261	2.814	2.435	1.39
1400	-6565.183	1.223	2.819	2.435	1.50
1500	-6565.190	1.229	2.787	2.435	

Table 6: Quantum Espresso energy cutoff behaviour

Cut-off Energy (eV)	Total Energy (eV)	Pressure (GPa)	$\epsilon_{\mathbf{ionic}}$	$\epsilon_{\mathbf{elec}}$	Frequency RMSS (cm^{-1})
680.3	-7510.348	2.782	2.837	2.454	0.97
816.3	-7510.423	2.424	2.854	2.454	0.68
952.4	-7510.524	2.513	2.827	2.453	0.23
1088.5	-7510.569	2.766	2.811	2.453	

Table 7: VASP cutoff energy behaviour

Cut-off Energy (eV)	Total Energy (eV)	Pressure (GPa)	$\epsilon_{\mathbf{ionic}}$	$\epsilon_{\mathbf{elec}}$	Frequency RMSS (cm^{-1})
500	-67.471	2.393	2.854	2.437	1.56
550	-67.485	2.445	2.834	2.437	1.42
600	-67.510	2.307	2.835	2.436	1.13
650	-67.530	2.259	2.836	2.435	0.86
700	-67.546	2.319	2.847	2.434	0.51
900	-67.560	2.676	2.855	2.434	

3 Optimization of the Dispersion Parameter

In the tables below the S_6 parameter of the Grimme dispersion correction and the S_R parameter of the TS correction were optimized to improve the agreement between the experimental and calculated unit-cell dimensions. The volume of the unit cell, percentage change in volume compared to experiment and the root mean squared fractional deviation (RMSFD) of the calculated unit-cell dimensions and angles from the experimental values are included.

Table 8: Crystal/TZVP/GD2 S_6 parameter optimization

S_6	Volume (Å^3)	ΔV(%)	RMSFD
No Correction	161.16	6.11	0.014
0.300	157.95	4.00	0.011
0.500	155.76	2.55	0.013
0.750	152.34	0.31	0.024
0.784	151.83	-0.03	0.026

Table 9: Crystal/DEF2/GD2 S_6 parameter optimization

S_6	Volume (Å^3)	ΔV(%)	RMSFD
No correction	163.89	7.91	0.018
0.400	159.19	4.81	0.011
0.500	158.04	4.05	0.010
0.600	157.15	3.47	0.011
0.700	155.55	2.42	0.014
0.750	154.72	1.87	0.018
0.800	153.78	1.25	0.021
0.850	151.18	0.86	0.022
0.900	152.25	0.24	0.026
0.920	151.87	-0.01	0.028
0.950	150.13	-1.15	0.033

Table 10: CASTEP/NCP17/GD2 S_6 parameter optimization

S_6	Volume (Å^3)	ΔV(%)	RMSFD
No correction	165.76	9.14	0.023
0.300	163.14	7.41	0.016
0.400	162.05	6.69	0.015
0.500	160.92	5.95	0.013
0.600	159.89	5.28	0.012
0.750	158.24	4.19	0.011
0.900	156.63	3.13	0.013
1.000	154.98	2.04	0.017
1.100	154.63	1.81	0.014
1.200	154.12	1.47	0.011
1.220	149.71	-1.43	0.038
1.240	149.39	-1.64	0.039
1.300	148.19	-2.43	0.042
1.400	146.33	-3.66	0.045

Table 11: CASTEP/NCP19/TS S_R parameter optimization

S_R	Volume (Å^3)	ΔV(%)	RMSFD
No correction	164.87	8.56	0.022
0.910	150.39	-0.98	0.011
0.916	150.96	-0.60	0.011
0.920	151.32	-0.37	0.011
0.925	151.74	-0.09	0.012
0.940	152.85	0.64	0.013

Table 12: Summary of optimized dispersion parameters

Method	Parameter	Optimized value
Crystal/DEF2/GD2-v	S_6	0.92
Crystal/DEF2/GD2-r	S_6	0.50
CASTEP/NCP19/GD3-v	S_6	Not valid
CASTEP/NCP19/TS-v	S_R	0.925

4 Program Settings

No projection of the translation modes was performed by the DFT programs in the calculation of the phonon modes. Apart from the settings mentioned below, all other settings were left at their default values.

4.1 Abinit

- Wavefunction convergence 1.0×10^{-12} Hartree
- Maximum force in geometry optimisation 1×10^{-5} Hartree/Bohr
- Phonon calculations using DFPT

4.2 CASTEP

- Wavefunction convergence 1.0×10^{-12} eV/atom
- Energy tolerance in optimisation 1.0×10^{-6} eV
- Force tolerance in optimisation 0.005 eV/Å
- Stress tolerance in optimisation 0.005 GPa
- Displacement tolerance in optimisation 2.0×10^{-4} Å
- Phonon calculations using DFPT for non-dispersion corrected calculations and numerical finite difference for dispersion corrected calculations

4.3 Crystal

- Wavefunction convergence for geometry optimisation 1.0×10^{-7} Hartree
- Wavefunction convergence for phonon calculation 1.0×10^{-10} Hartree
- Root means squared displacement tolerance in optimisation 1.2×10^{-4} Bohr
- Integration tolerances set using;
  TOLINTEG
  8 8 8 8 16

- Phonon calculations using numerical differentiation and intensities calculation using a coupled Hartree-Fock approach

4.4 QE

- Wavefunction convergence for geometry optimisation 1.0×10^{-10} Rydberg
- Wavefunction convergence for phonon calculation 1.0×10^{-14} Rydberg
- Energy threshold for convergence in optimisation 1.0×10^{-7} Rydberg
- Force threshold for convergence in optimisation 1.0×10^{-6} Rydberg/Bohr
- Phonon and intensities using DFPT

4.5 VASP

- PREC flag = Accurate
- Tetrahedron method with Blochl corrections and a smear width of 0.05 eV
- Projection performed in reciprocal space
- Wavefunction convergence for geometry optimisation 1.0×10^{-8} eV
- Wavefunction convergence for phonon calculation 1.0×10^{-8} eV
- Maximum force for geometry optimisation 5.0×10^{-4} eV/Å
- Phonon and the dielectric constant calculations use DFPT for non-dispersion corrected calculations and numerical differentiation for dispersion corrected methods

5 Optimised Unit Cells

The unit cell and atom positions were fully optimised maintaining space group symmetry.

Table 13: Calculated unit cell dimensions using no dispersion correction[a]

Method	a (Å)	b (Å)	c (Å)	α (°)	β (°)	γ (°)	Volume (Å^3)	O-O (Å)
Abinit/FHI	4.935	5.839	6.068	100.6	103.3	100.0	162.9	1.501
Abinit/ONCVPSP	4.923	5.792	6.158	101.3	102.7	98.6	164.5	1.503
CASTEP/NCP19	4.923	5.797	6.164	101.3	102.6	98.6	164.9	1.500
Crystal/TZVP	4.904	5.662	6.209	101.3	103.7	97.1	161.6	1.564
Crystal/DEF2	4.899	5.759	6.193	101.1	102.7	98.2	164.1	1.507
QE/SSSP	4.902	5.758	6.158	101.3	102.7	98.3	163.0	1.502
VASP/PAW	4.894	5.739	6.162	101.3	102.8	98.2	162.3	1.509

Table 14: Calculated unit cell dimensions using dispersion corrections[a]

Method	a (Å)	b (Å)	c (Å)	α (°)	β (°)	γ (°)	Volume (Å^3)	O-O (Å)
Abinit/FHI/GD2	4.785	5.598	6.058	100.9	103.2	98.1	152.2	1.4996
Abinit/ONCVPSP/GD2	4.800	5.623	6.120	101.3	102.9	97.6	155.2	1.501
CASTEP/NCP19/GD2	4.776	5.610	6.178	101.0	102.4	96.7	156.6	1.501
CASTEP/NCP19/GD3	4.813	5.639	6.161	101.2	103.3	97.1	157.1	1.498
CASTEP/NCP19/GD3-BJ	4.797	5.623	6.142	101.0	102.7	97.3	156.2	1.498
CASTEP/NCP19/TS	4.741	5.557	6.240	102.8	104.4	96.4	152.8	1.497
CASTEP/NCP19/TS-v	4.746	5.538	6.211	102.8	104.4	96.4	151.7	1.497
Crystal/TZVP/GD2	4.732	5.423	6.330	101.2	104.4	94.6	153.0	1.565
Crystal/DEF2/GD2	4.732	5.530	6.278	101.0	103.3	95.5	155.2	1.509
Crystal/DEF2/GD2-v	4.692	5.425	6.357	101.3	104.4	94.3	152.4	1.509
Crystal/DEF2/GD2-r	4.796	5.617	6.215	100.8	102.6	96.5	158.5	1.508
Crystal/DEF2/GD3-BJ	4.779	5.590	6.173	101.0	103.2	97.0	155.2	1.506
QE/SSSP/GD2	4.760	5.587	6.175	100.9	102.5	96.5	155.3	1.503
VASP/PAW/GD2	4.761	5.603	6.151	101.0	102.5	97.0	155.0	1.510
VASP/PAW/GD3	4.775	5.629	6.150	100.9	103.3	97.4	155.4	1.508
VASP/PAW/GD3-BJ	4.790	5.615	6.103	101.2	103.0	97.7	154.2	1.507
VASP/PAW/TS	4.730	5.568	6.165	102.3	103.7	96.9	151.6	1.505

6 Translational Invariance

The frequencies of the 3 acoustic modes calculated without the imposition of any sum-rules are presented in Table 16. Calculations were performed using each package and its associated pseudo-potential or basis set, with and without dispersion correction. Default grids were used for all packages except CASTEP. It was found that for CASTEP the value of FINE_GRID_SCALE keyword had a significant effect on the magnitude of the acoustic mode frequencies at the gamma point (Table 15). The CASTEP results presented in the paper and the supplementary information have been calculated with FINE_GRID_SCALE=6.

Table 15: CASTEP root mean squared error (RMSE) of the acoustic modes

FINE_GRID_SCALE	RMSE
3	21.6
4	15.1
5	8.1
6	4.6

Table 16: Frequencies[a] of the acoustic modes (cm^{-1})

Method	Mode 1	Mode 2	Mode 3
Abinit/FHI	-29.5	-12.4	22.0
Abinit/FHI/GD2	-28.6	-22.3	-15.1
Abinit/ONCVPSP	14.4	24.1	28.7
Abinit/ONCVPSP/GD2	15.9	30.0	33.5
Castep/NCP19	-4.8	2.4	6.7
Castep/NCP19/GD2	-3.5	-0.8	6.1
Castep/NCP19/GD3	-5.3	-2.9	4.6
Castep/NCP19/GD3-BJ	-3.7	0.9	4.5
Castep/NCP17/TS	6.0	7.2	8.6
Castep/NCP17/TS-v	4.4	5.0	8.9
Crystal/TZVP	-3.1	-2.4	-2.1
Crystal/TZVP/GD2	-3.2	-2.5	-2.1
Crystal/DEF2	-3.5	-2.8	-2.6
Crystal/DEF2/GD2	-3.6	-2.8	-2.3
Crystal/DEF2/GD2-v	-3.2	-2.7	-2.4
Crystal/DEF2/GD2-r	-3.4	-2.8	-2.3
Crystal/DEF2/GD3-BJ	-3.3	-2.8	-2.3
QE/SSSP	-5.8	12.3	16.8
QE/SSSP/GD2	-8.8	-5.0	11.1
VASP/PAW	-1.5	-0.7	-0.5
VASP/PAW/GD2	-1.2	-0.8	-0.5
VASP/PAW/GD3	-2.1	-0.8	-0.7
VASP/PAW/GD3-BJ	-1.7	-1.0	-0.7
VASP/PAW/TS	-1.6	-1.1	-0.7

[a] Negative numbers indicate an imaginary frequency

From each of the calculations reported in Table 16 the root mean squared error (RMSE) in the frequencies of the three acoustic modes at the gamma point, as calculated by each package, without imposing translational invariance was calculated. It should be noted that all frequency calculations used the average of the naturally occurring isotope masses.

7 Calculated Frequencies and Intensities

7.1 Frequencies and intensities with no dispersion correction

Figures 1 and 2 show a comparison of the non-dispersion corrected calculations of frequencies and intensities for the intermediate (300-750 cm^{-1}) and high (above 750 cm^{-1}) regions of the spectrum.

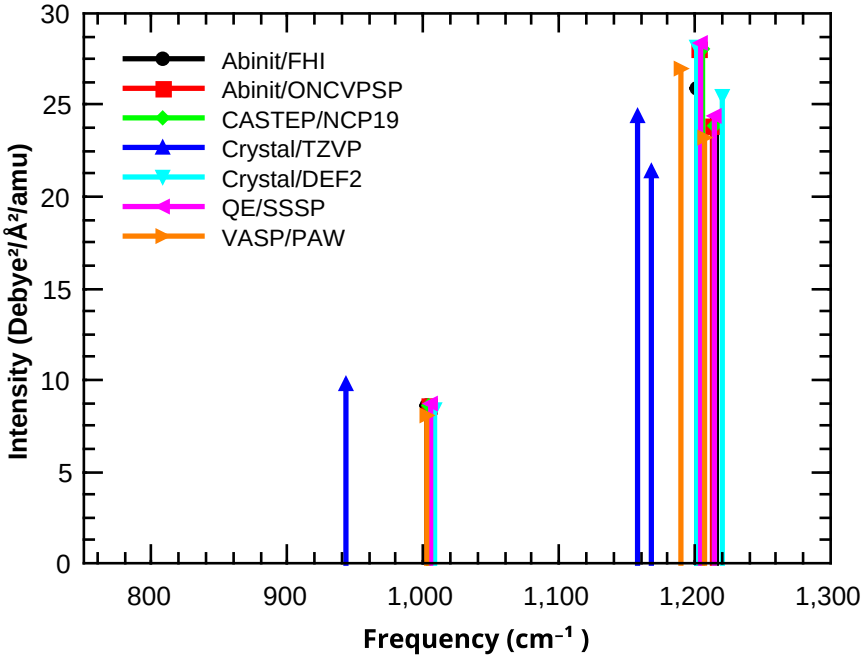

Figure 1: Frequencies and Intensities (no dispersion correction)- High Frequency Range

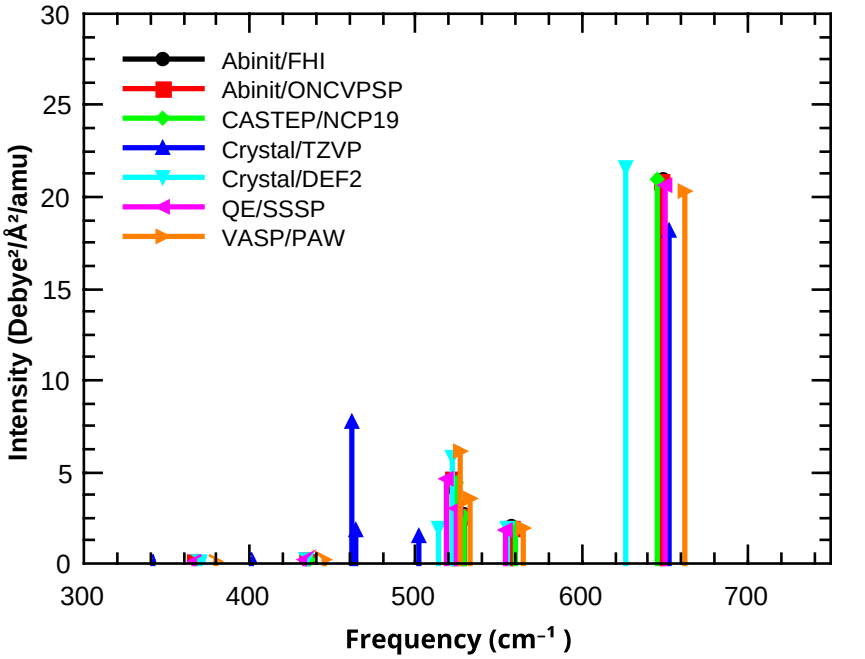

Figure 2: Frequencies and Intensities (no dispersion correction) - Intermediate Frequency Range

7.2 Abinit Frequencies and Intensities

Figure 3 shows the frequencies and intensities calculated by Abinit.

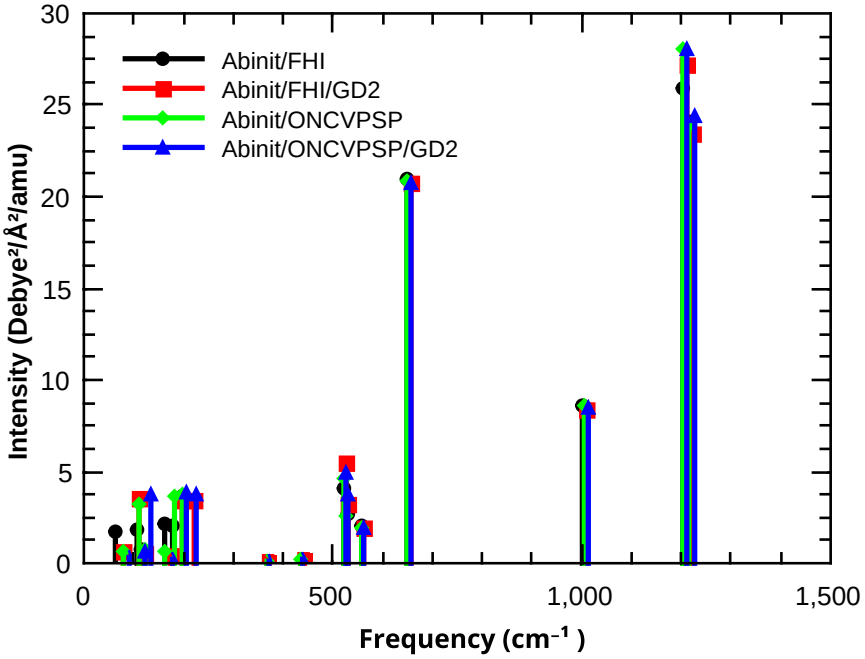

Figure 3: Abinit Frequencies and Intensities

7.3 CASTEP Frequencies and Intensities

Figure 4 shows the frequencies and intensities calculated by CASTEP.

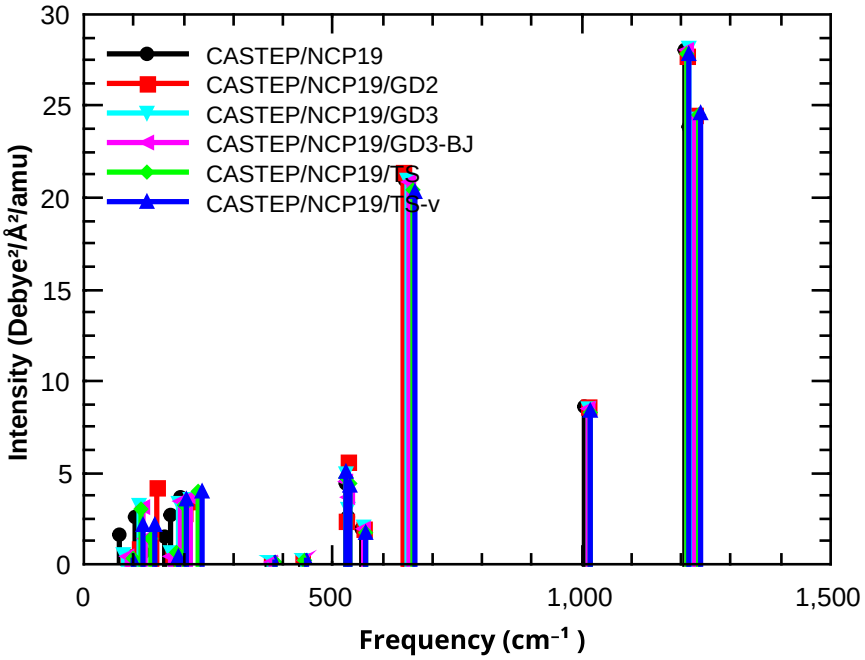

Figure 4: CASTEP Frequencies and Intensities

7.4 Crystal Frequencies and Intensities

Figure 5 shows the frequencies and intensities calculated by Crystal.

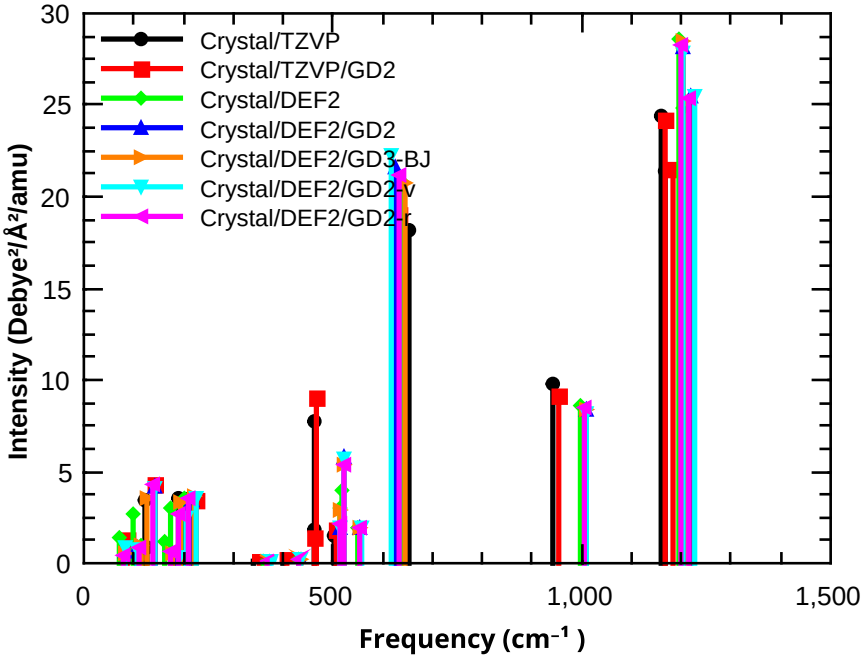

Figure 5: Crystal Frequencies and Intensities

7.5 QE Frequencies and Intensities

Figure 6 shows the frequencies and intensities calculated by Quantum Espresso.

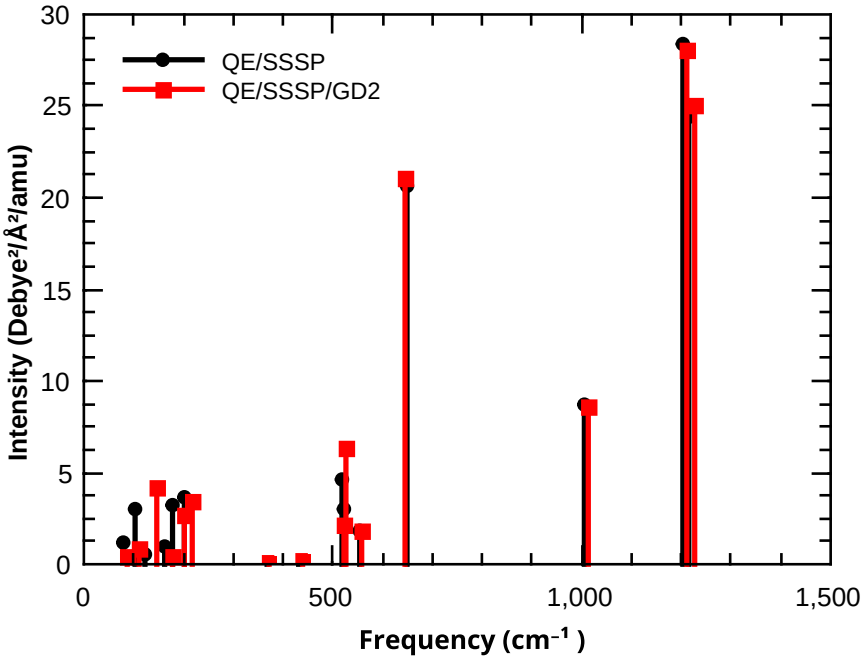

Figure 6: QE Frequencies and Intensities

7.6 VASP Frequencies and Intensities

Figure 7 shows the frequencies and intensities calculated by VASP.

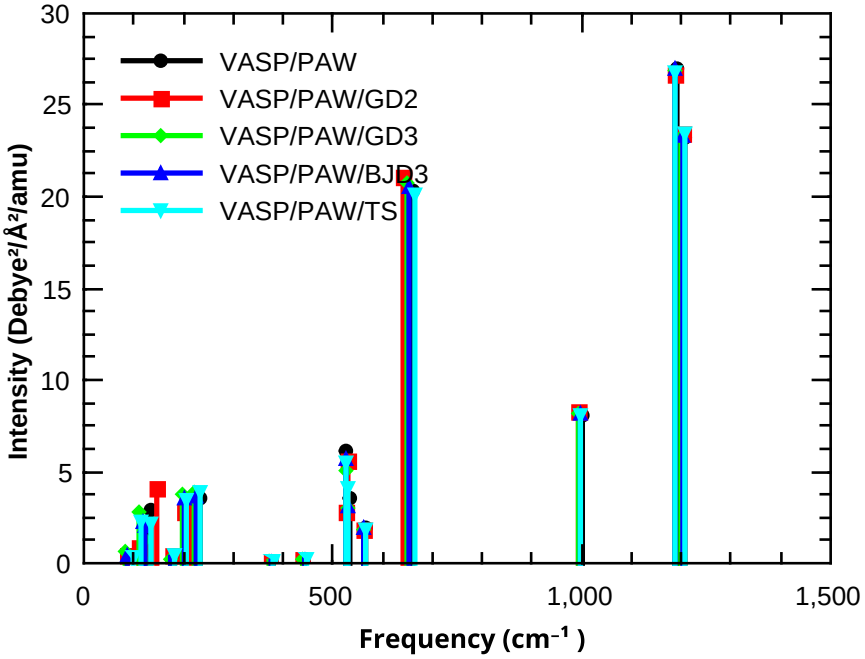

Figure 7: VASP Frequencies and Intensities

8 Phonon Mode Analysis

In order to understand the contributions internal and external modes and specific groups of atoms make to the phonon modes an analysis of the Crystal/DEF2 calculation has been made using the PDielec package to determine the percentage energy contribution for the different components to each mode. Figure 8 shows the breakdown of each mode in terms of external (centre of mass and rotational) motion and internal (vibrational) motion for the case that the S_2O_8 is treated as a single moeity.

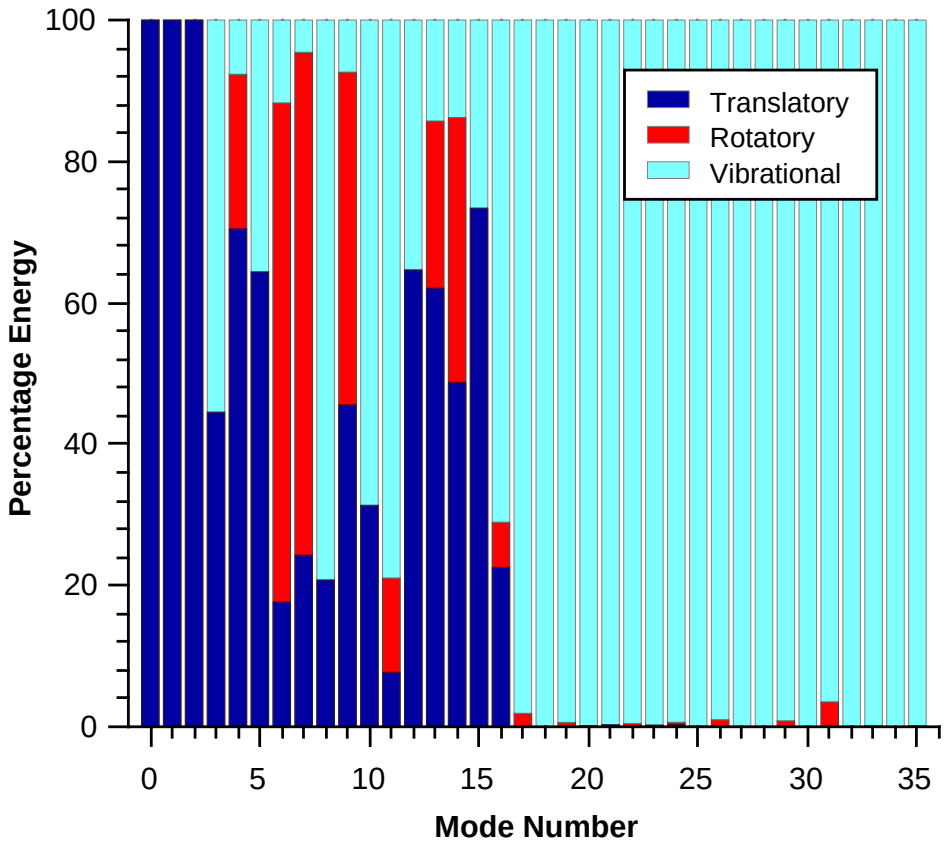

Figure 8: Internal and External Contributions to the Phonon Modes using S_2O_8

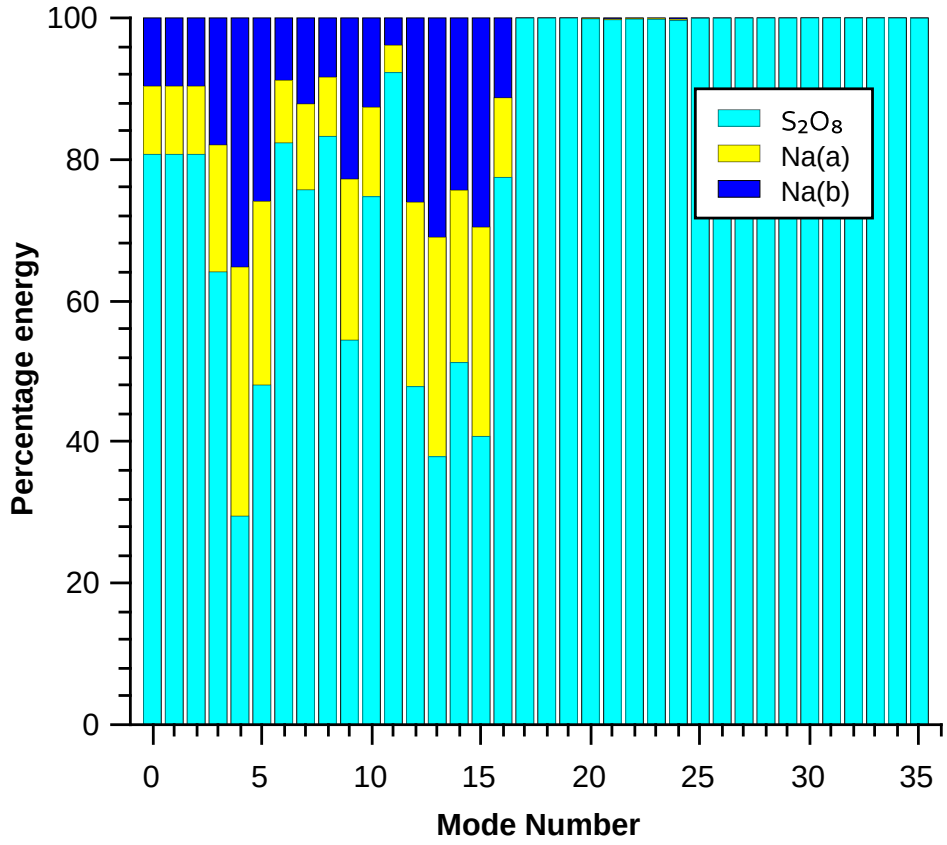

Figure 9: 'Molecular' Contributions to the Phonon Modes using S_2O_8

The frequencies of the normal modes for this calculation are shown in Table 17.

Table 17: Mode numbering and frequencies of the Crystal/DEF2 calculation

Mode	Frequency cm^{-1}	Mode	Frequency cm^{-1}
0	0.00	18	360.81
1	0.00	19	384.39
2	0.00	20	429.51
3	72.34	21	513.30
4	81.15	22	514.15
5	99.45	23	518.90
6	103.56	24	530.26
7	108.94	25	550.68
8	116.08	26	601.20
9	117.77	27	638.05
10	161.65	28	703.50
11	166.26	29	809.34
12	176.10	30	998.29
13	184.42	31	1028.08
14	194.37	32	1194.18
15	201.37	33	1197.69
16	220.23	34	1204.06
17	321.91	35	1229.36

9 Maxwell-Garnett effective medium theory

All spectra reported were calculated using PDielec from the normal modes and Born charges using a Maxwell-Garnett effective medium theory model for 10% by volume of small crystallites embedded in a PTFE matrix support. The Lorentzian line width for the calculation was taken to be 5 cm^{-1}.

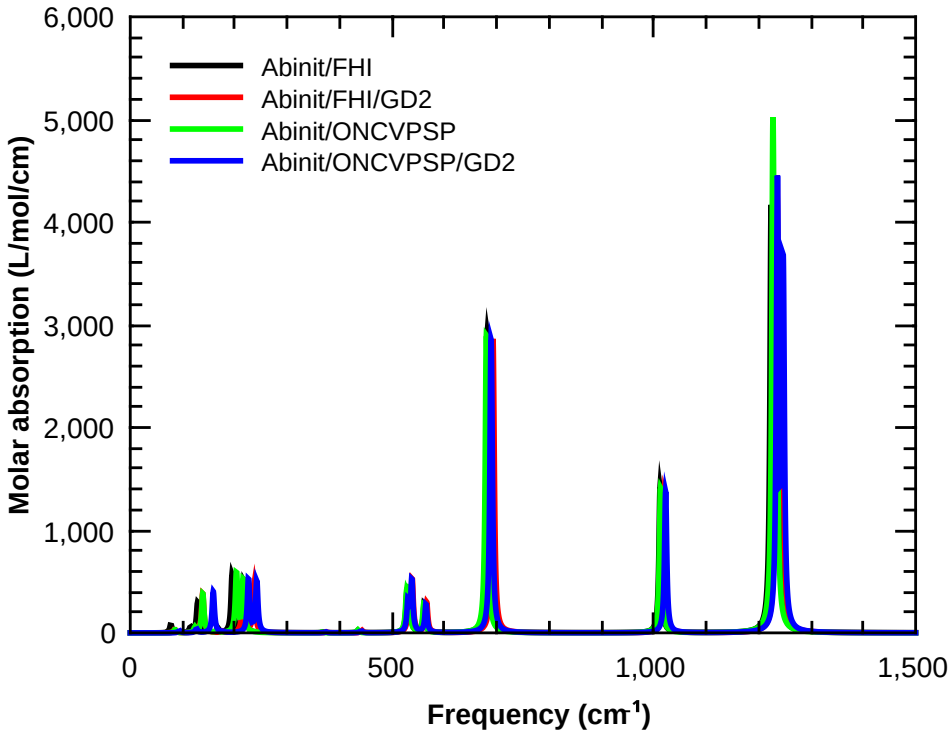

Figure 10: Abinit IR Spectra - Full Frequency Range

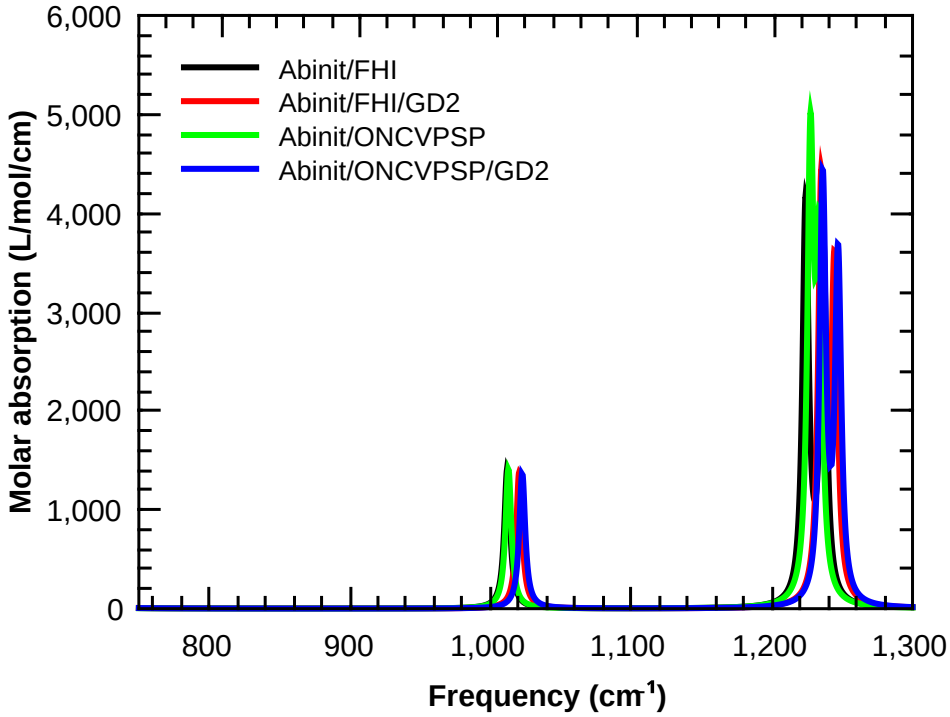

Figure 11: Abinit IR Spectra - High Frequency Range

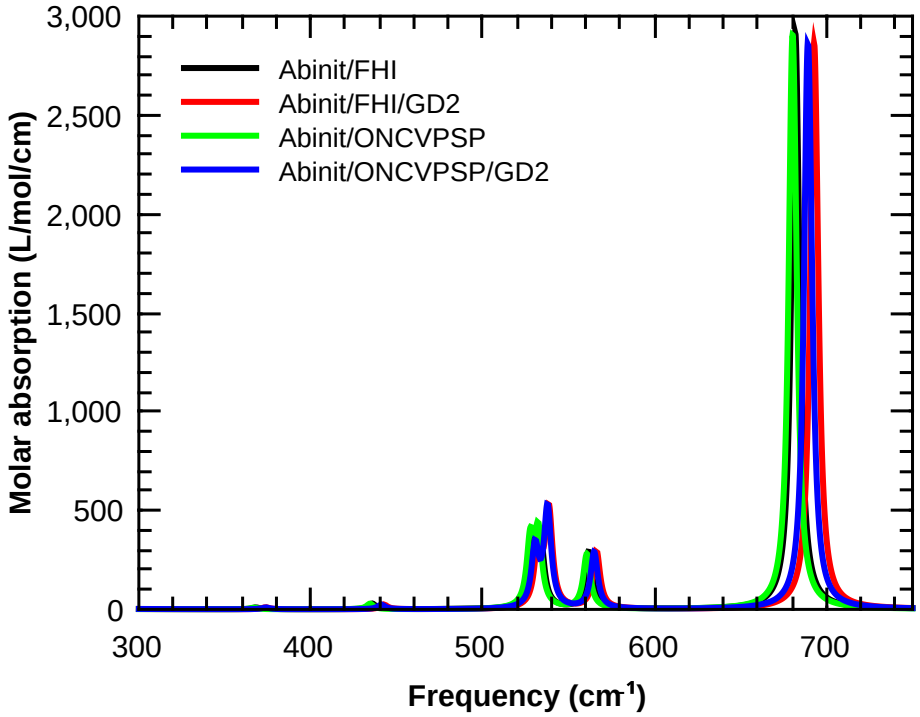

Figure 12: Abinit IR Spectra - Intermediate Frequency Range

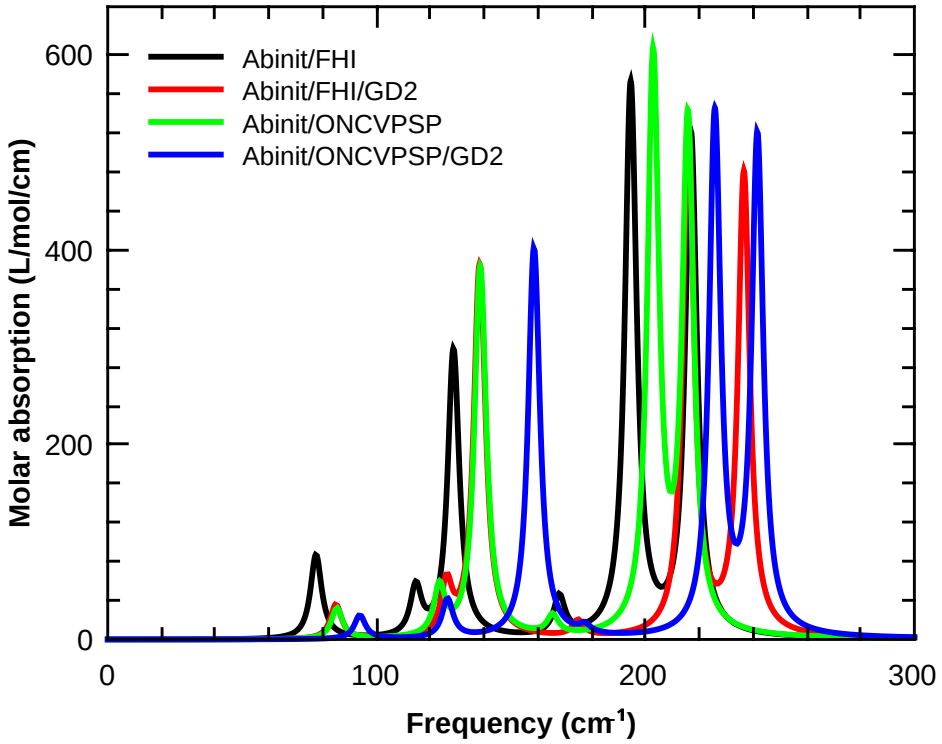

Figure 13: Abinit IR Spectra - Low Frequency Range

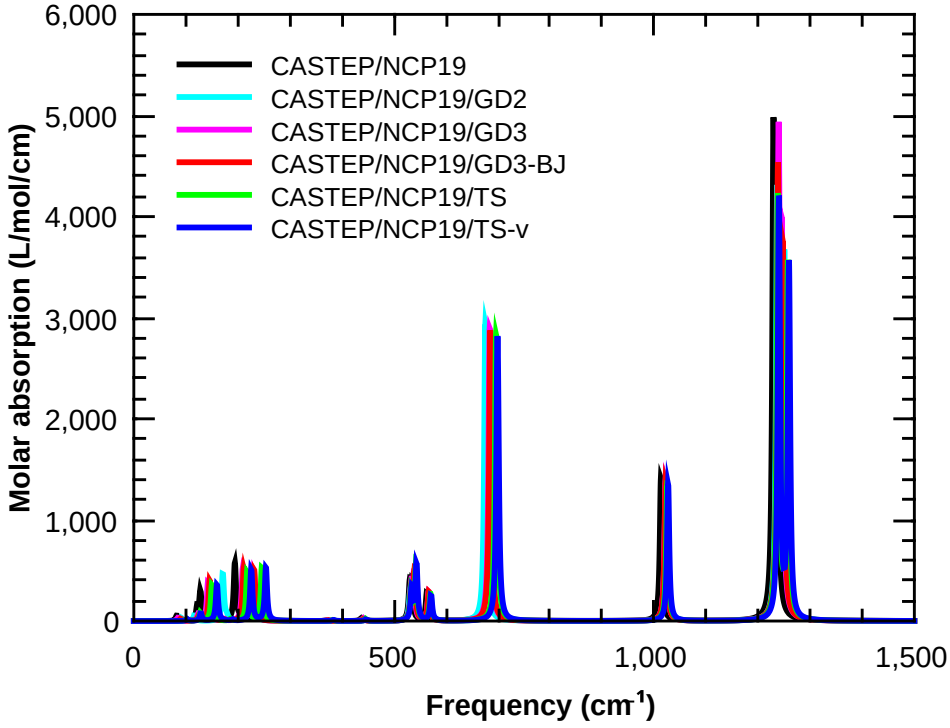

Figure 14: CASTEP IR Spectra - Full Frequency Range

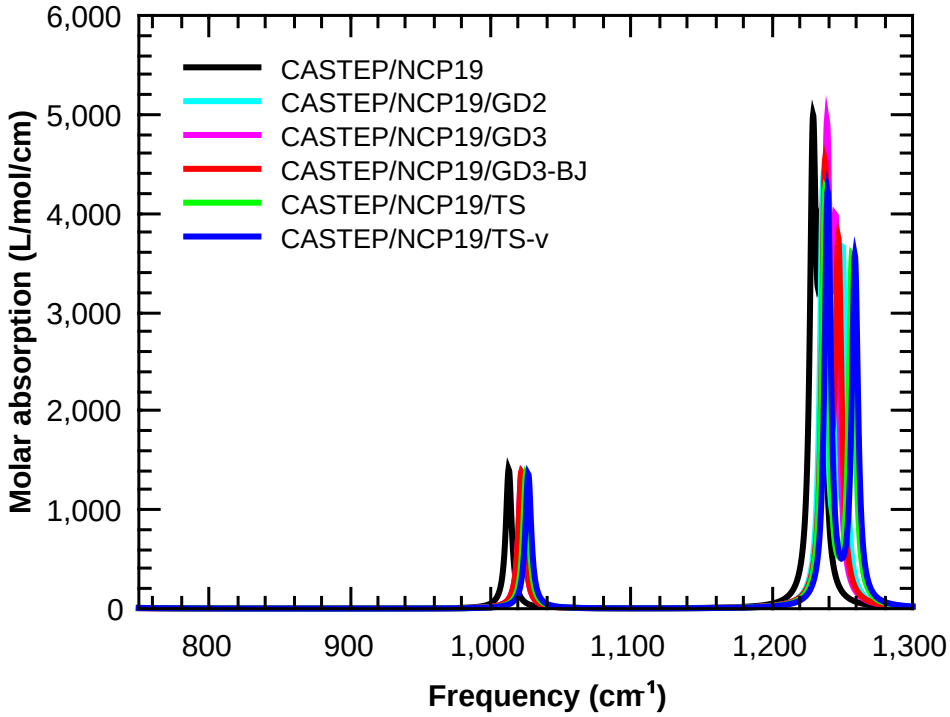

Figure 15: CASTEP IR Spectra - High Frequency Range

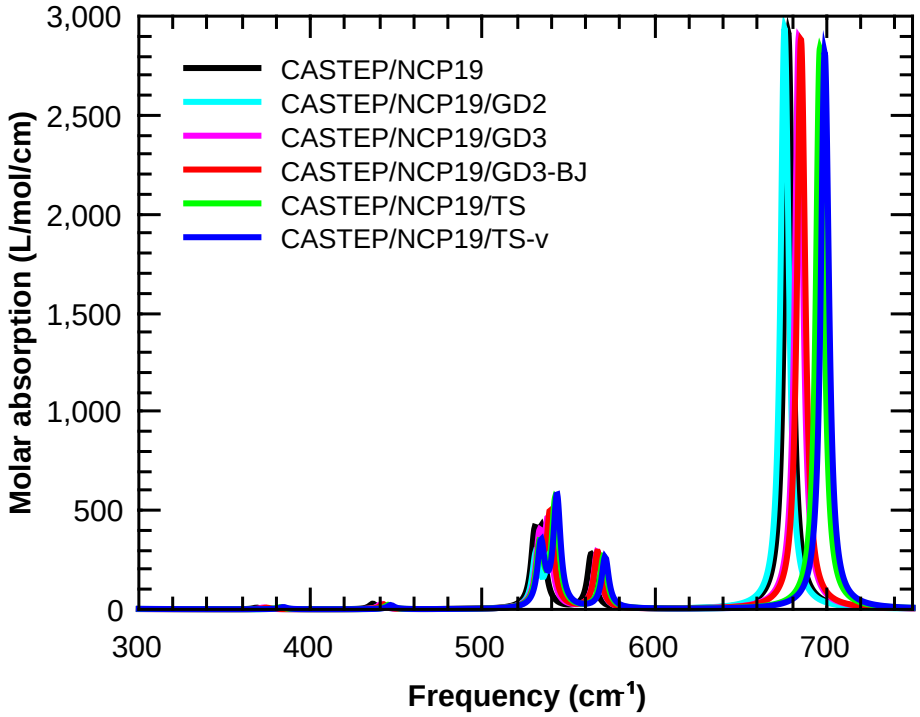

Figure 16: CASTEP IR Spectra - Intermediate Frequency Range

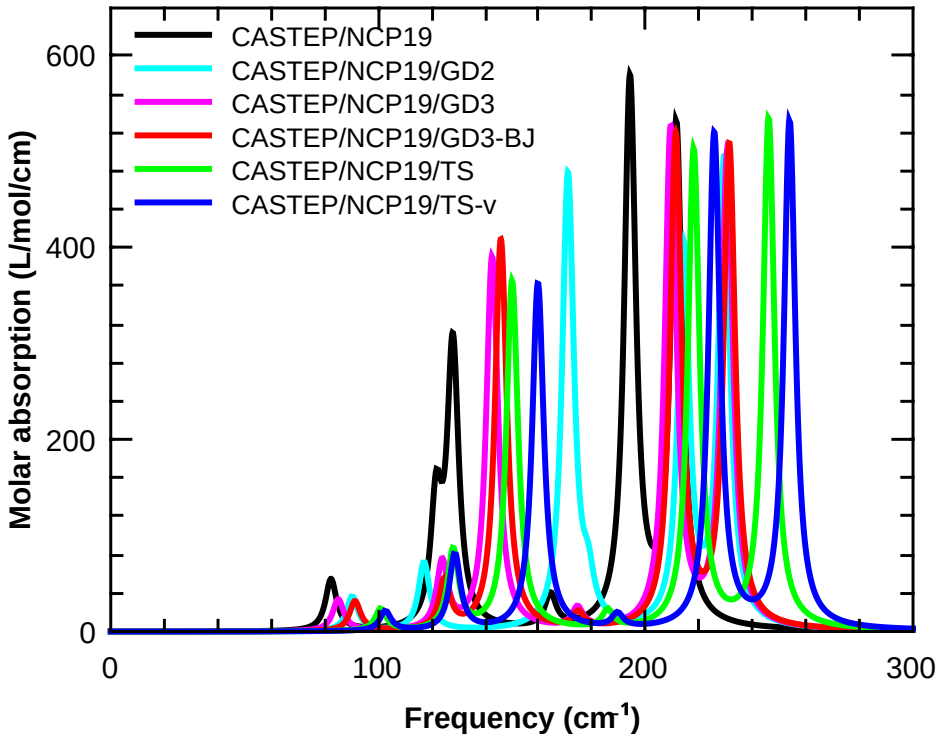

Figure 17: CASTEP IR Spectra - Low Frequency Range

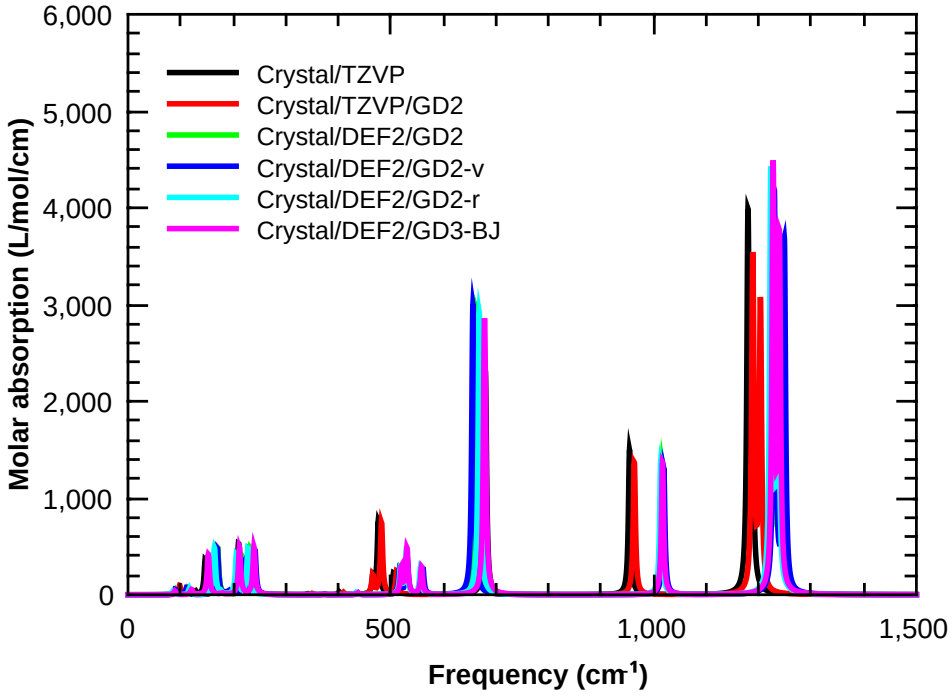

Figure 18: Crystal IR Spectra - Full Frequency Range

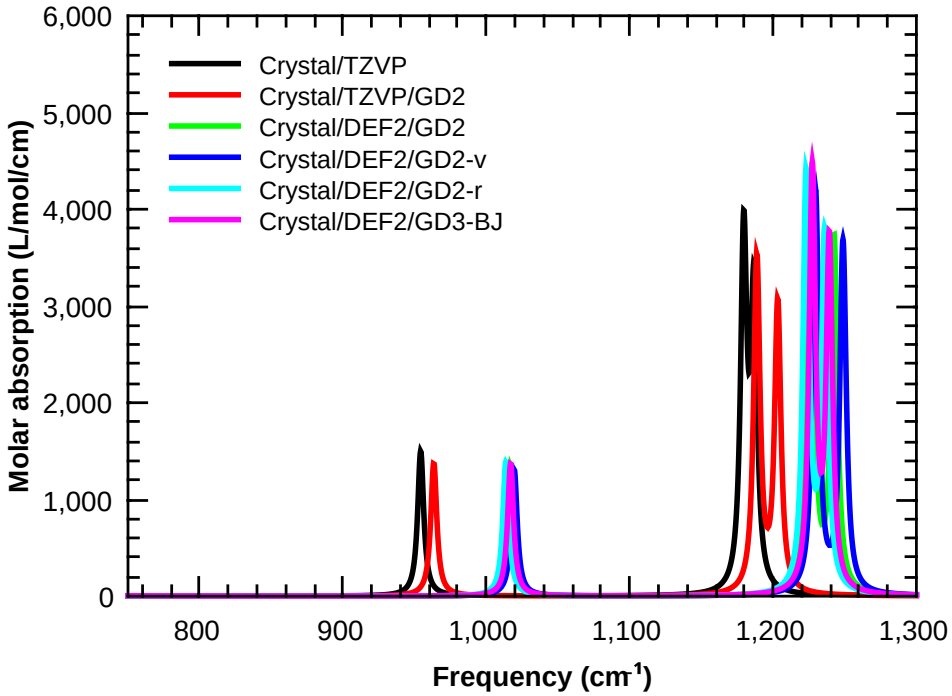

Figure 19: Crystal IR Spectra - High Frequency Range

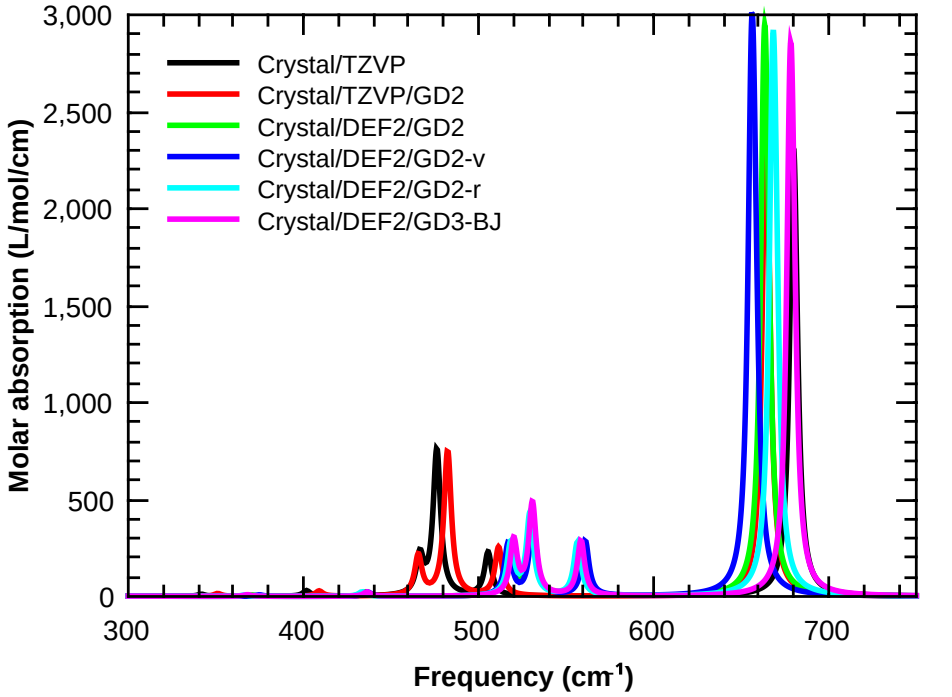

Figure 20: Crystal IR Spectra - Intermediate Frequency Range

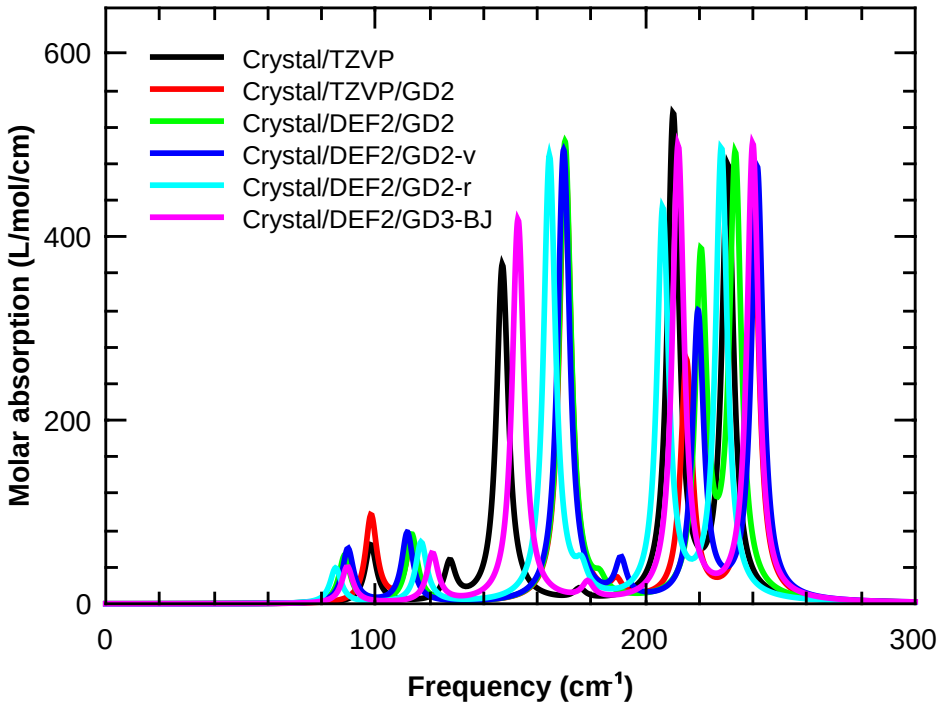

Figure 21: Crystal IR Spectra - Low Frequency Range

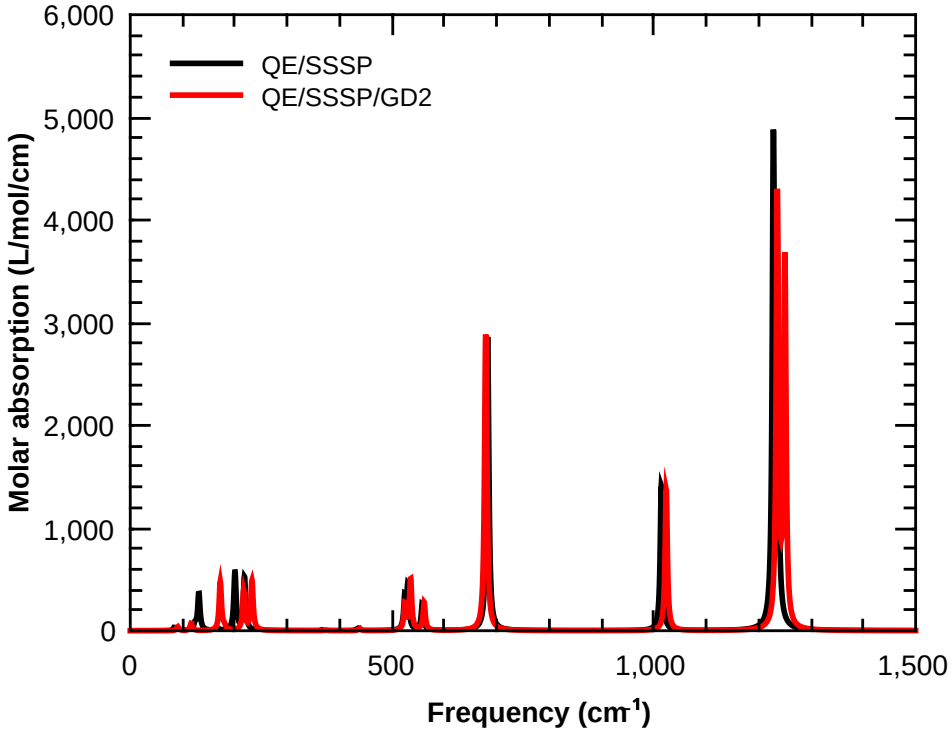

Figure 22: QE IR Spectra - Full Frequency Range

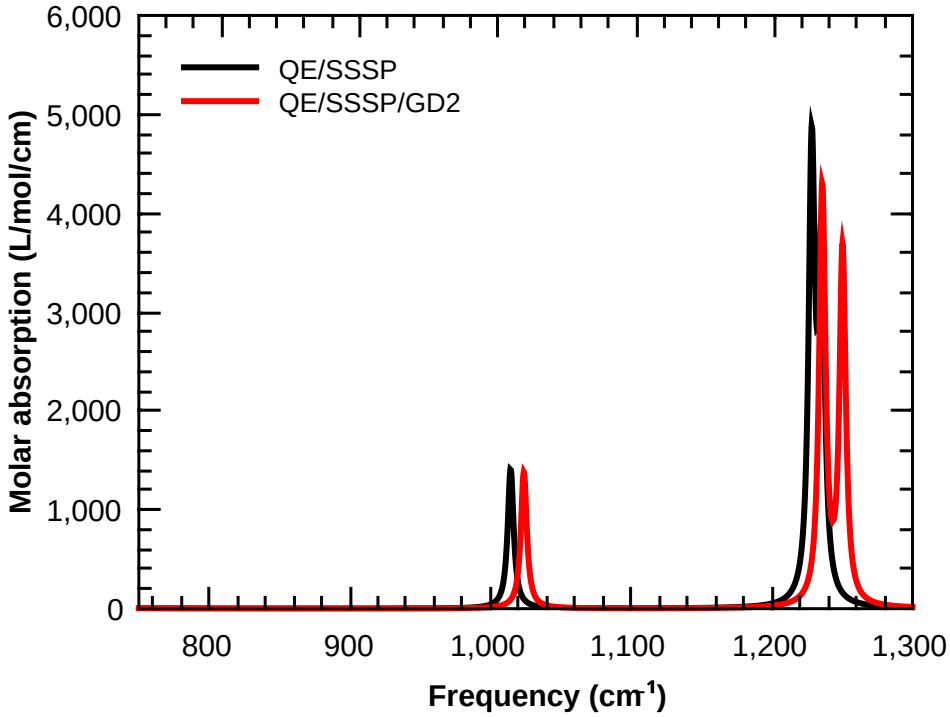

Figure 23: QE IR Spectra - High Frequency Range

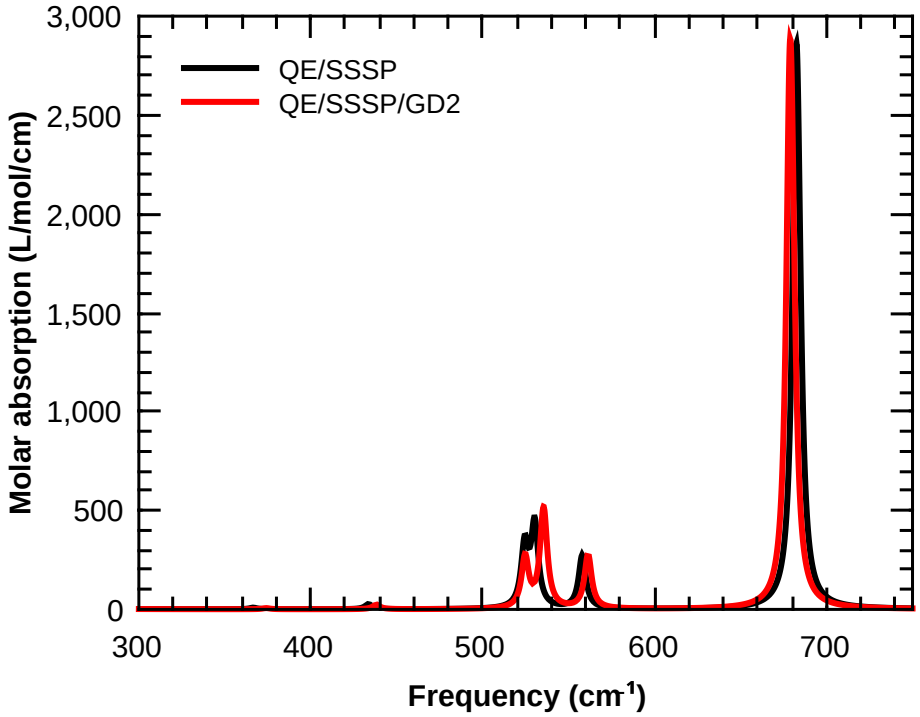

Figure 24: QE IR Spectra - Intermediate Frequency Range

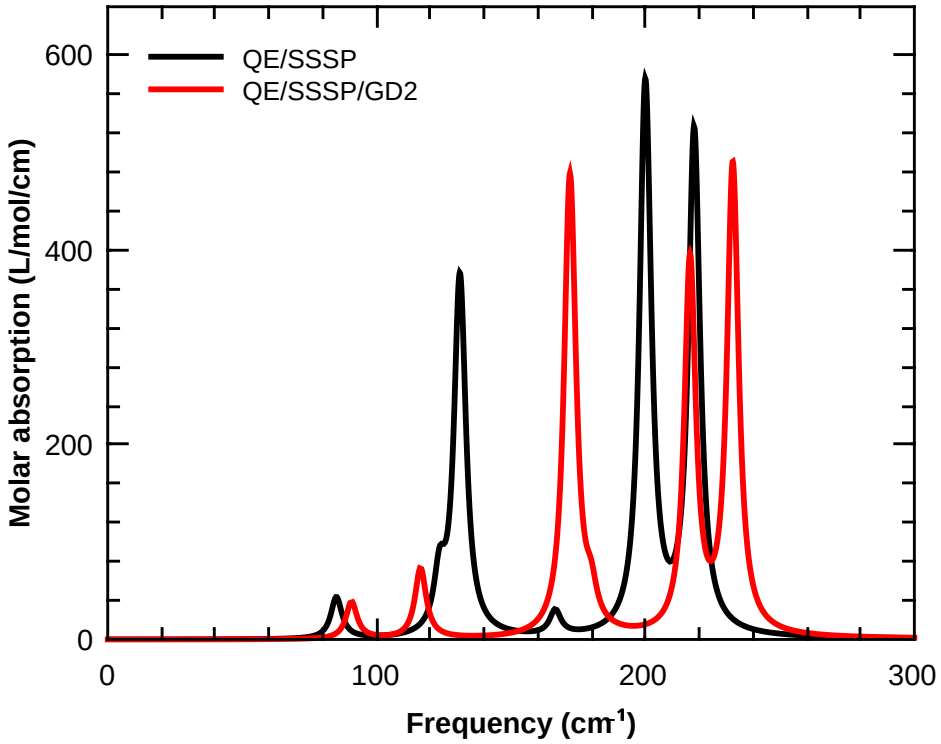

Figure 25: QE IR Spectra - Low Frequency Range

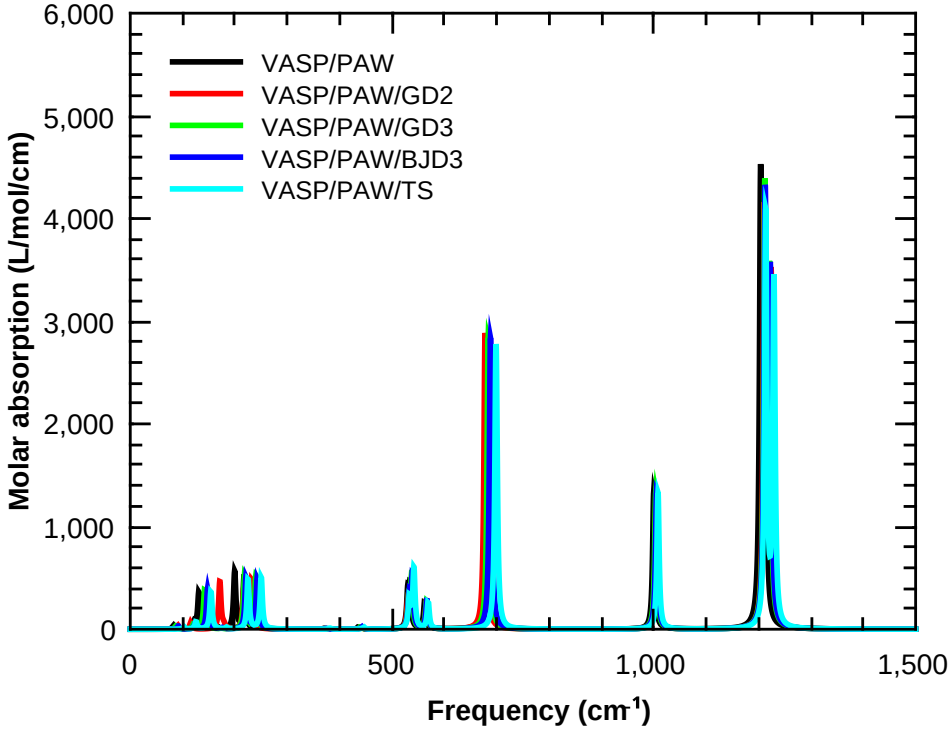

Figure 26: VASP IR Spectra - Full Frequency Range

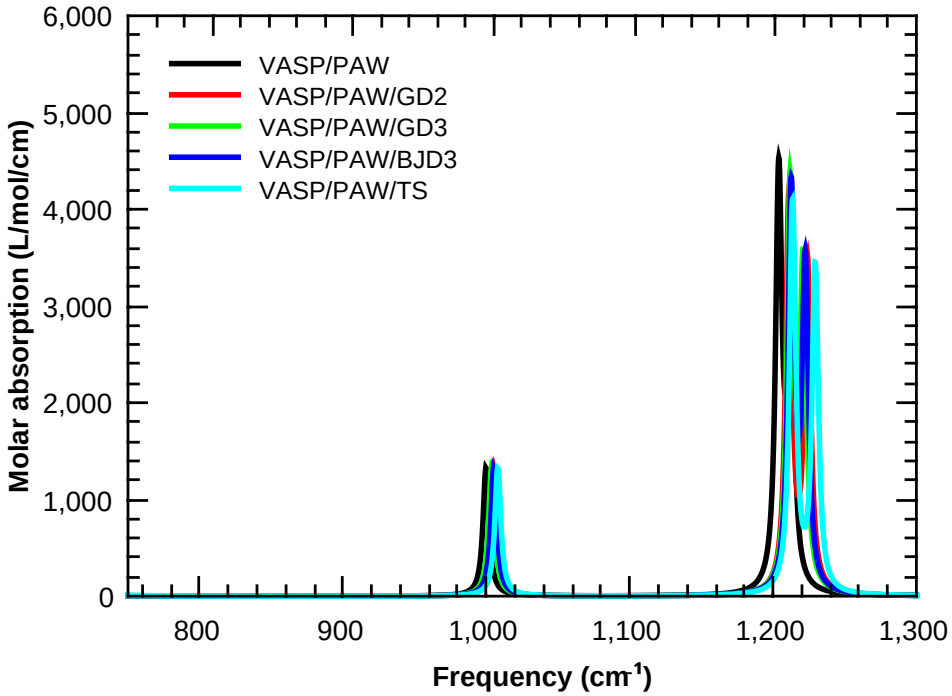

Figure 27: VASP IR Spectra - High Frequency Range

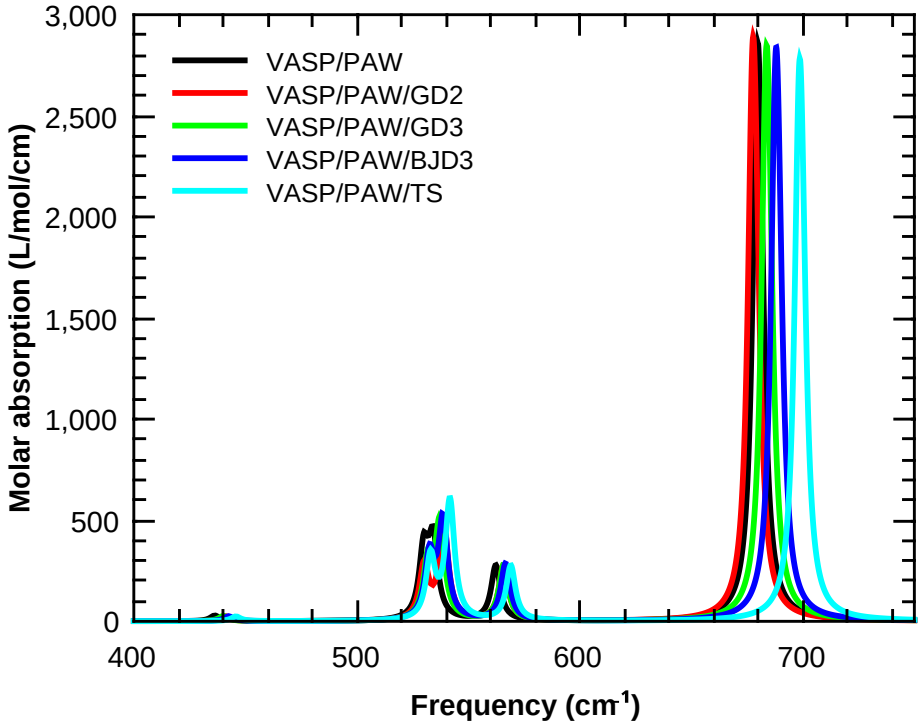

Figure 28: VASP IR Spectra - Intermediate Frequency Range

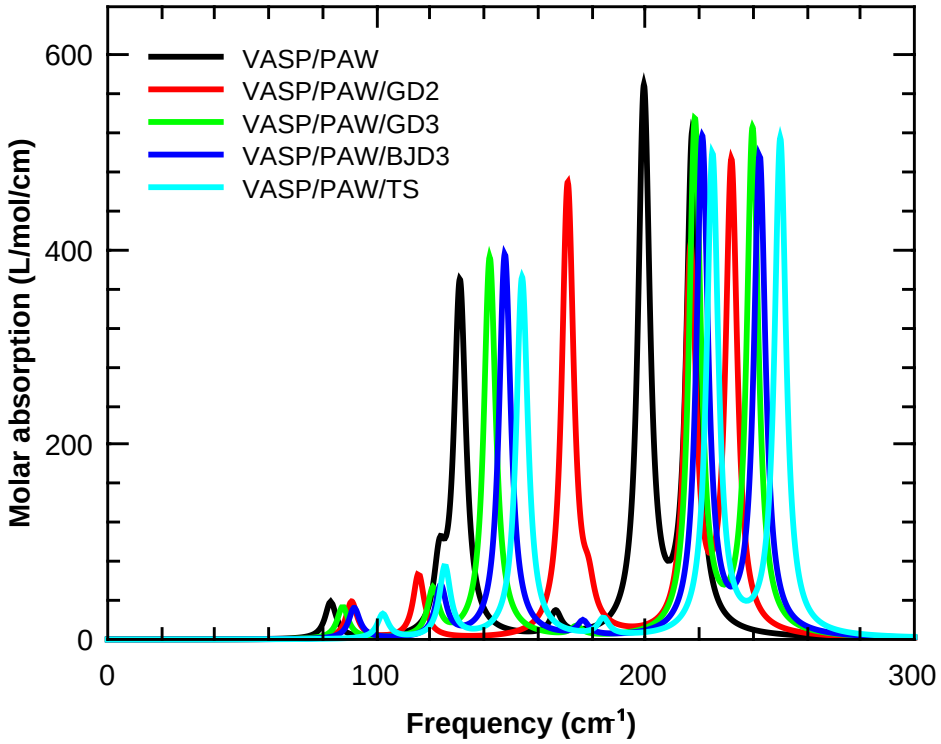

Figure 29: VASP IR Spectra - Low Frequency Range

10 Comparison of Calculated Spectra

The calculated spectra were compared with each other by calculating the normalized cross-correlation coefficient between each pair of spectra. This calculation also provides a 'lag' or frequency shift which maximizes the cross-correlation for each pair of spectra. Figure 30 shows the calculated cross-correlation coefficients for the complete frequency range. The cross-correlation matrix is symmetric and the results presented using a gap-map where yellow is used to describe the highest cross-correlation coefficient and blue the lowest with the methods have being clustered according to their similarity. The clustering is made clear by the dendrogram at the top of the heat map. The heat map itself shows the values of the cross-correlation coefficient as a colour map. In Figures 30 to 33 the absorption spectra used in the cross-correlation was calculated using a Maxwell-Garnett effective medium description of 10% by volume of sodium peroxodisulfate in PTFE with a line broadening factor of $5\,\mathrm{cm}^{-1}$. Figure 31 shows a gap-map created by using the lag frequency to calculate the similarity of each method. The lag frequencies in this plot have been calculated using the full frequency range of the spectra. The lag frequencies vary between -40 and +40 cm^{-1}. The low frequency range of the spectra appears to be particularly sensitive to the method of calculation. So gap-maps were also created based only the low frequency range of the spectra (below 300 cm^{-1}. Figure 32 shows the heat map calculated using the normalized cross-correlations coefficients. Figure 33 shows the associated lag coefficients as a gap-map.

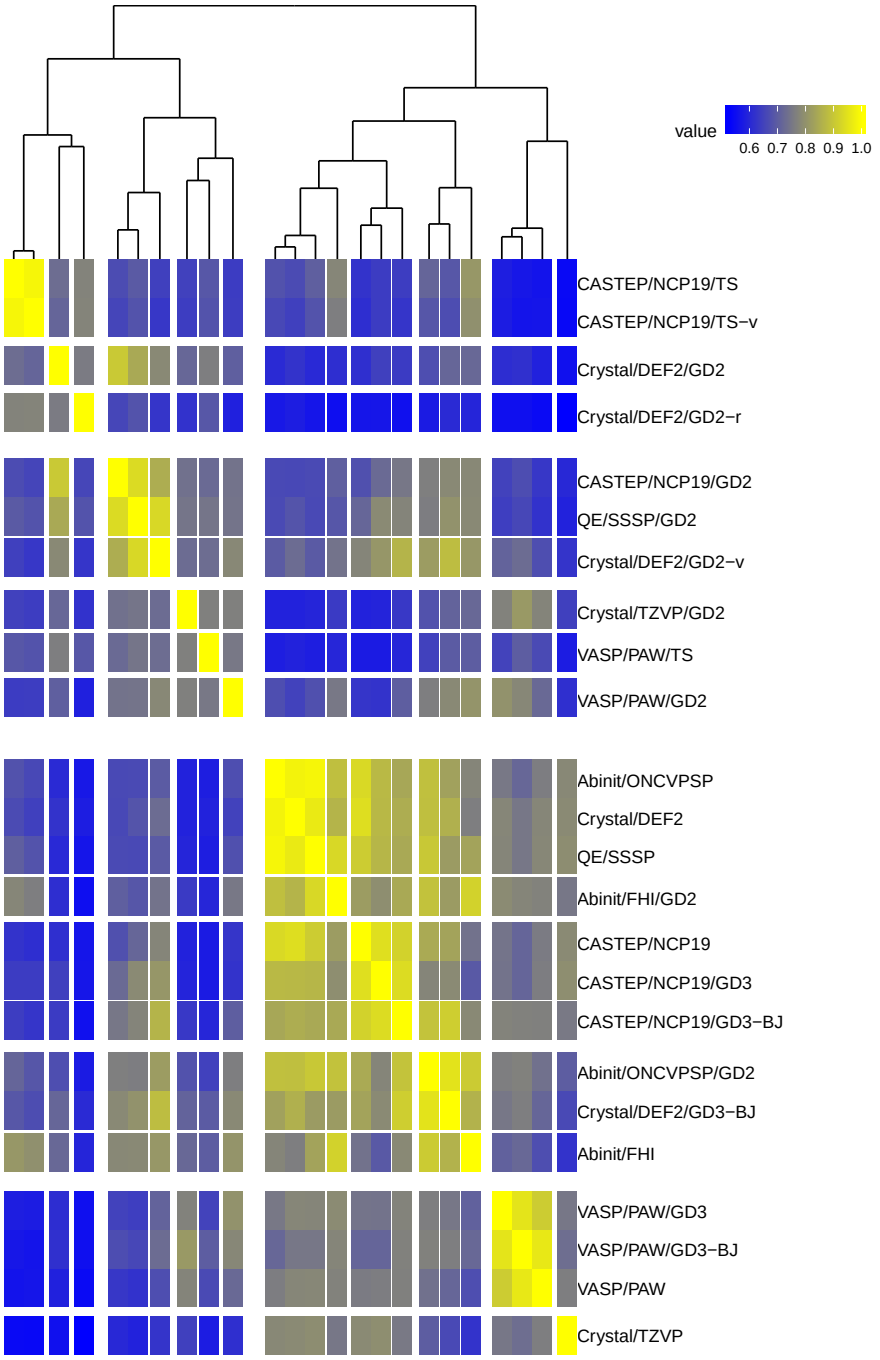

Figure 30: Cross-correlation heat-map of full frequency absorption spectra after clustering

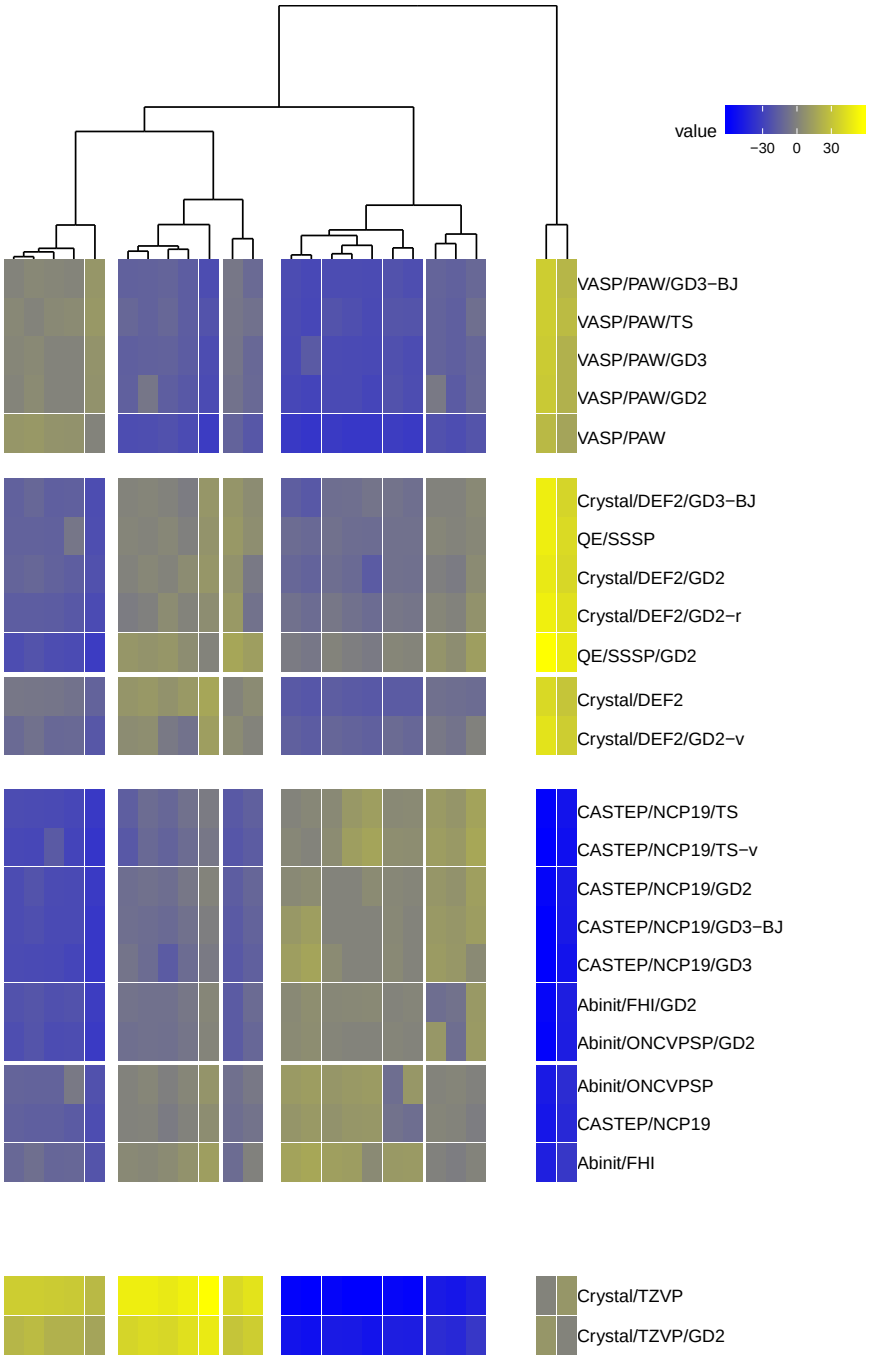

Figure 31: Frequency lag heat-map of full frequency absorption spectra after clustering

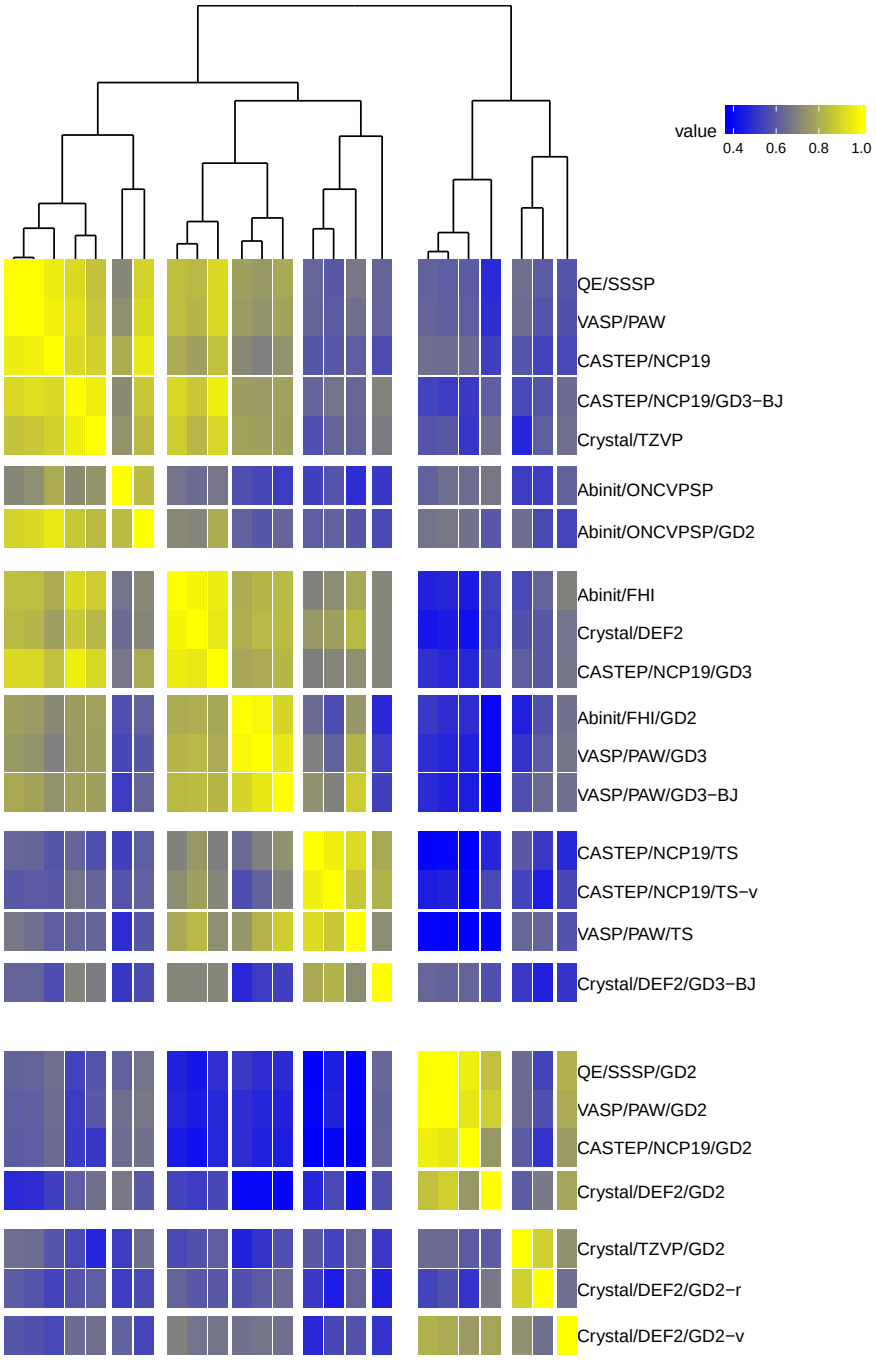

Figure 32: Cross-correlation heat-map of low frequency absorption spectra after clustering

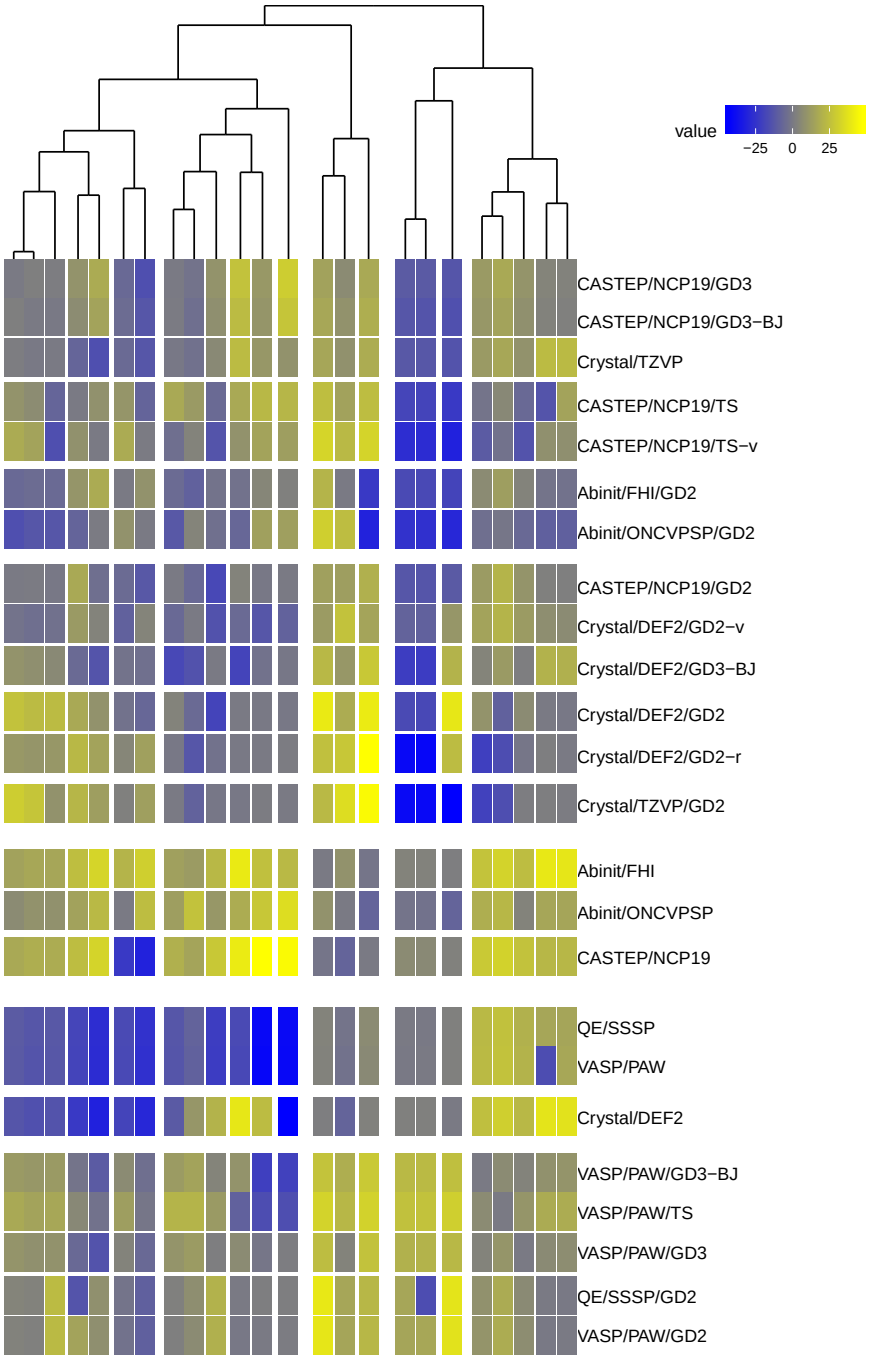

Figure 33: Frequency lag heat-map of low frequency absorption spectra after clustering

11 Comparison of Effective Medium Theories

Figures 34 to 37 compare the molar absorption spectra calculated using an Averaged Permittivity at low concentrations with the Maxwell-Garnett and Bruggeman effective medium theories at a concentration of 10% volume fraction of sodium peroxodisulfate supported in PTFE with a Lorentzian width factor of $5\,\mathrm{cm}^{-1}$.

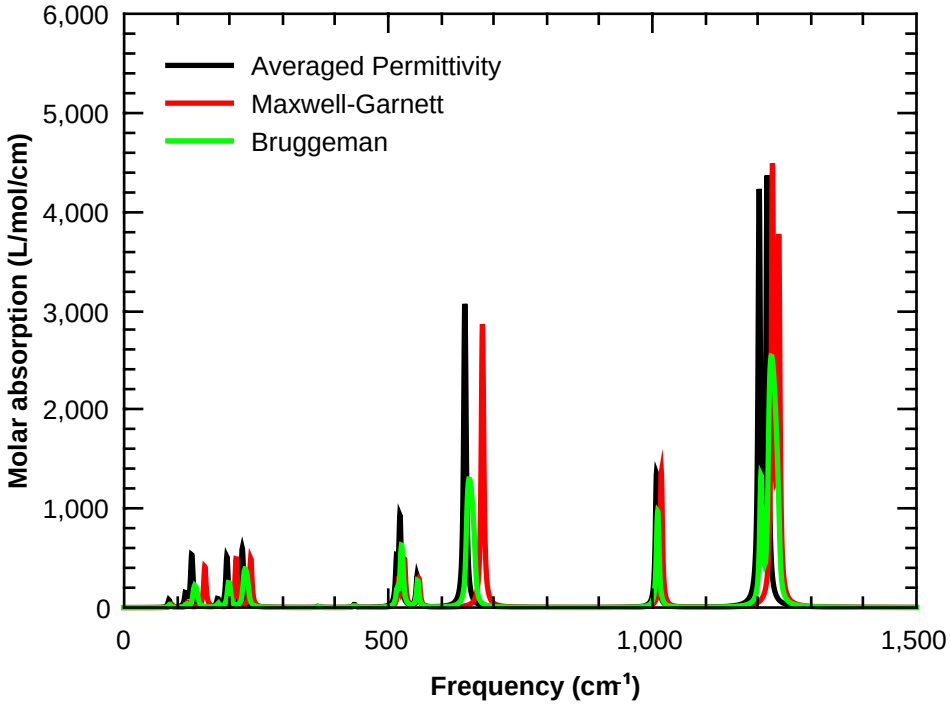

Figure 34: Average Permittivity, Maxwell-Garnett and Bruggeman Molar Absorption from Crystal/DEF2/GD3-BJ, full frequency range

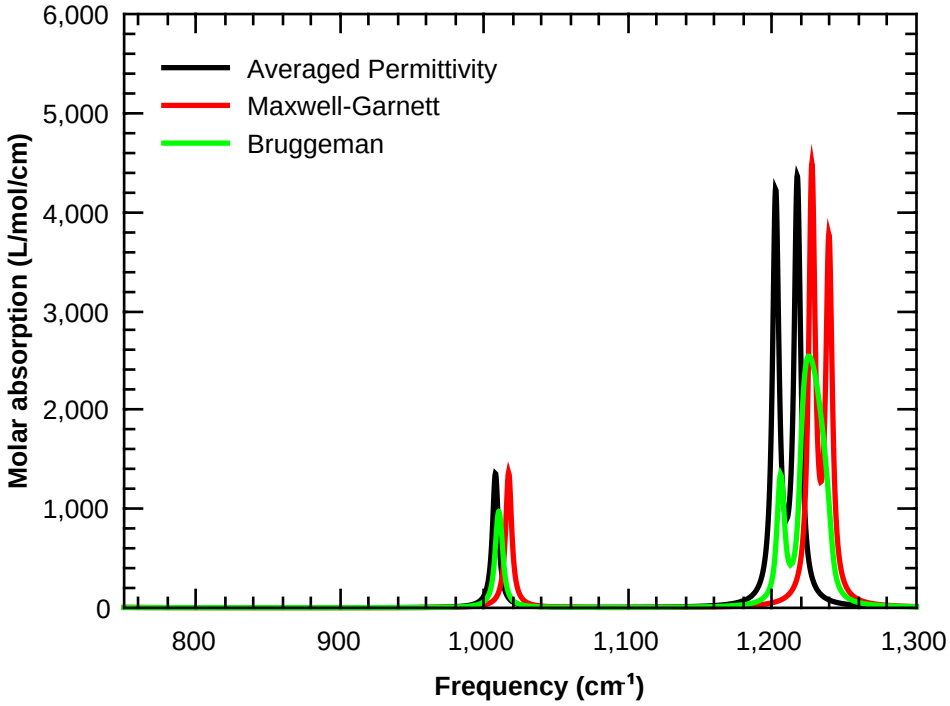

Figure 35: Average Permittivity, Maxwell-Garnett and Bruggeman Molar Absorption from Crystal/DEF2/GD3-BJ, high frequency range

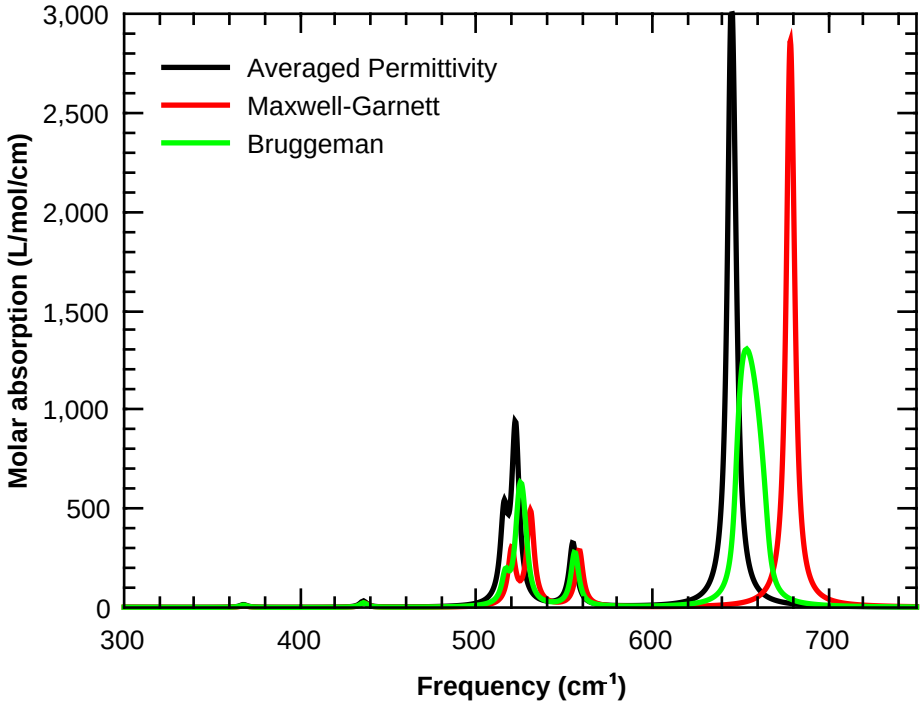

Figure 36: Average Permittivity, Maxwell-Garnett and Bruggeman Molar Absorption from Crystal/DEF2/GD3-BJ, intermediate frequency range

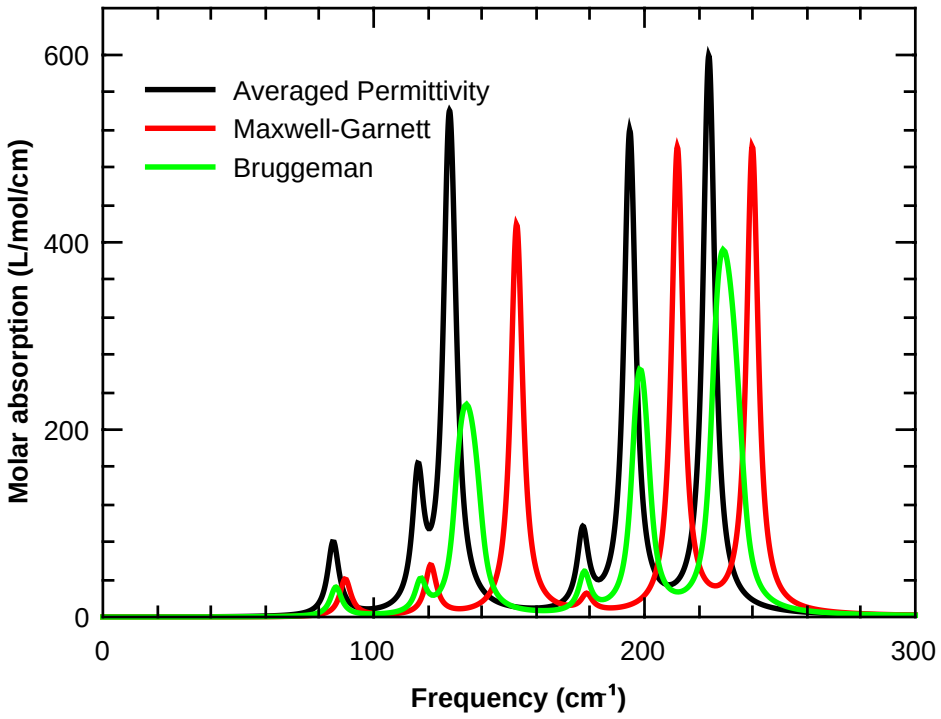

Figure 37: Average Permittivity, Maxwell-Garnett and Bruggeman Molar Absorption from Crystal/DEF2/GD3-BJ, low frequency range

12 Mie Scattering from Spherical Particles

When the wavelength of light is similar to or smaller than the particles being studied. Scattering of light by the particles has to be considered. For spherical particles this can be described well using Mie scattering theory, as long as no multiple scattering takes place. In other words the particles must be very dilute. The spectra shown in Figures 39 and 40 were obtained from the VASP/GD3-BJ phonon calculations using the PDielec package. A 10% volume fraction of spheres in PTFE was used with a Lorentzian line width of $5\,\mathrm{cm}^{-1}$. The smallest particle size (0.1 µm) results for Mie scattering coincide with those of the Maxwell-Garnett method. As the particle size increases the higher frequencies are more affected and the absorption broadens.

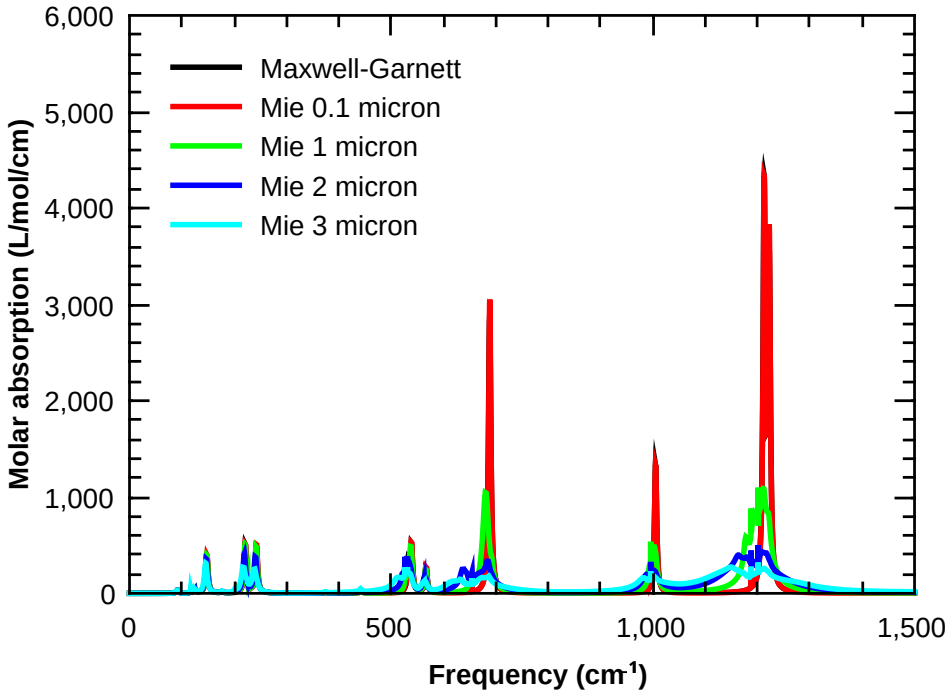

Figure 38: Calculated Infrared Spectra Incorporating Mie Scattering - full frequency range

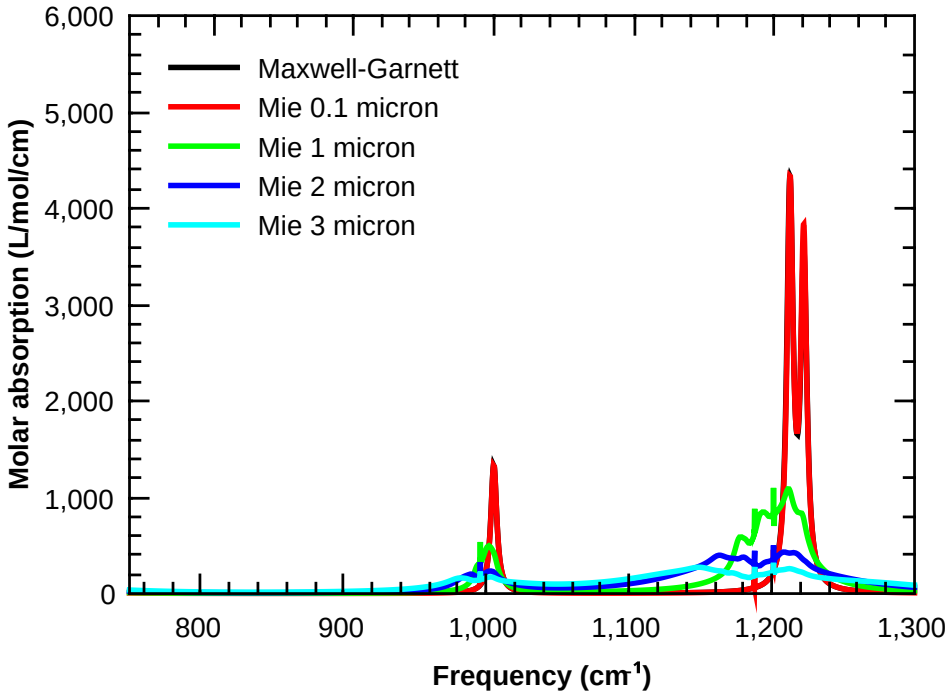

Figure 39: Calculated Infrared Spectra Incorporating Mie Scattering - high frequency range. This is the same as Figure 17 in the main paper

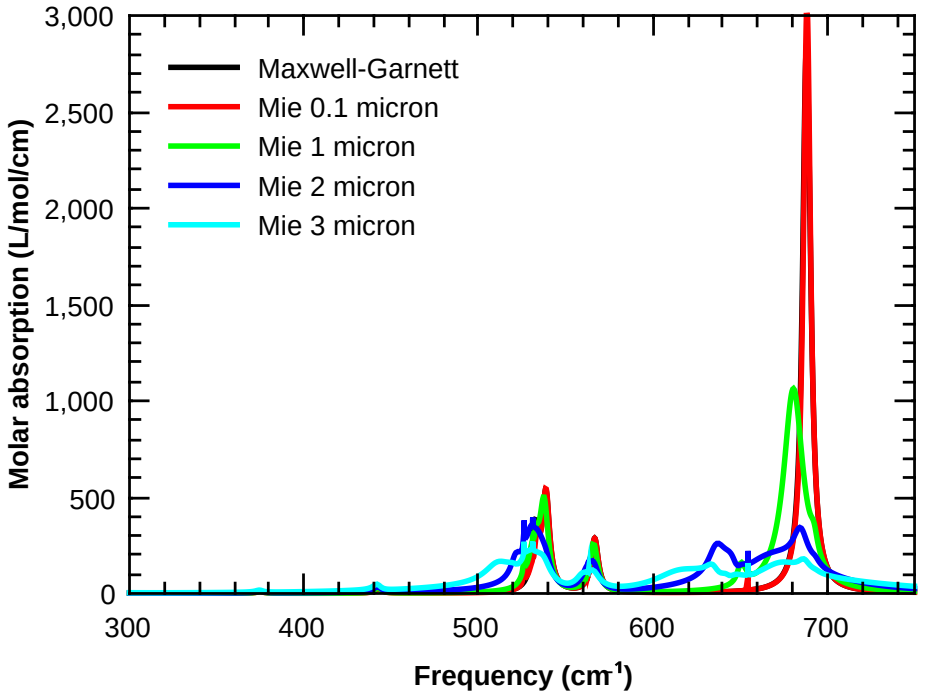

Figure 40: Calculated Infrared Spectra Incorporating Mie Scattering - intermediate frequency range. This is the same as Figure 17 in the main paper

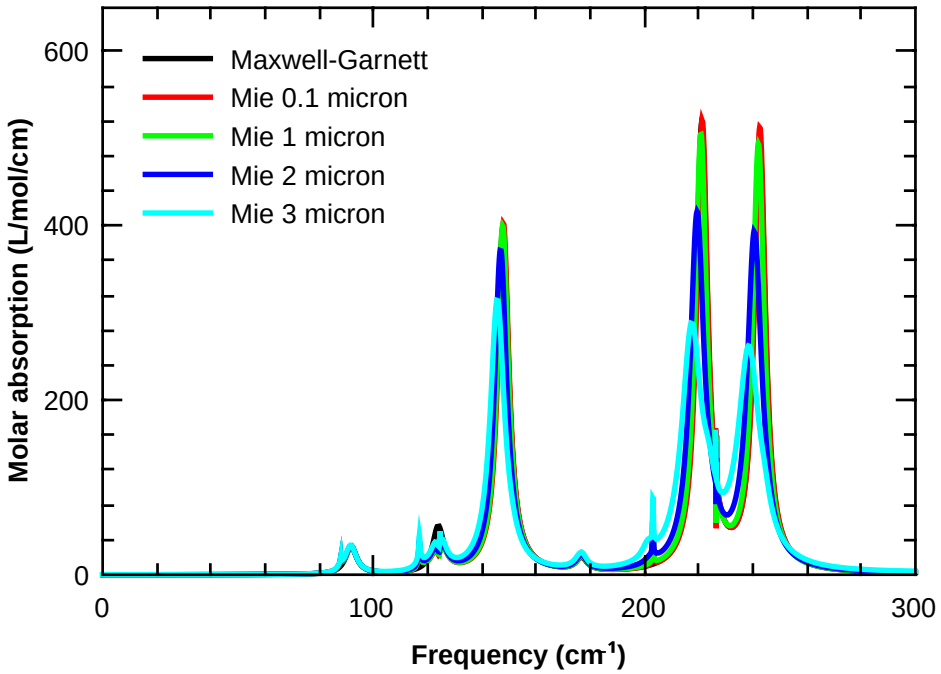

Figure 41: Calculated Infrared Spectra Incorporating Mie Scattering - low frequency range

13 ATR Spectra

The ATR spectra were calculated using a composite material consisting of a 50% volume fraction of sodium peroxodisulfate and air on a slab of diamond with a refractive index of 2.4. The angle of incidence of the incoming radiation was 45° and the radiation was assumed to have equal S and P polarization. All the results presented used the Bruggeman method to calculate the permittivity of the effective medium with a width factor of $30\,\mathrm{cm}^{-1}$.

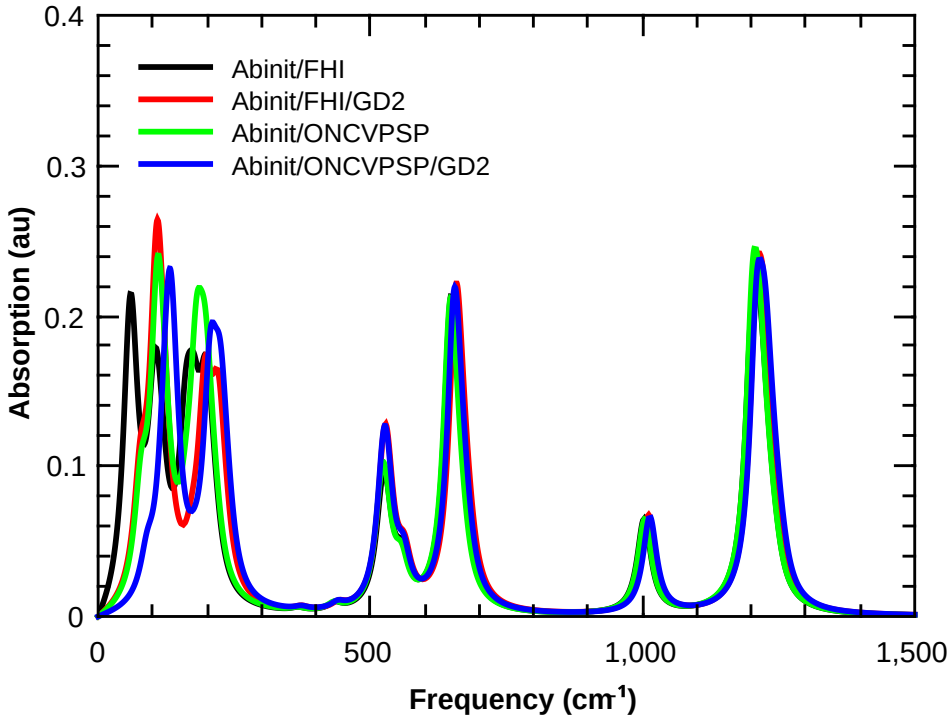

Figure 42: Abinit ATR Spectra - Full Frequency Range

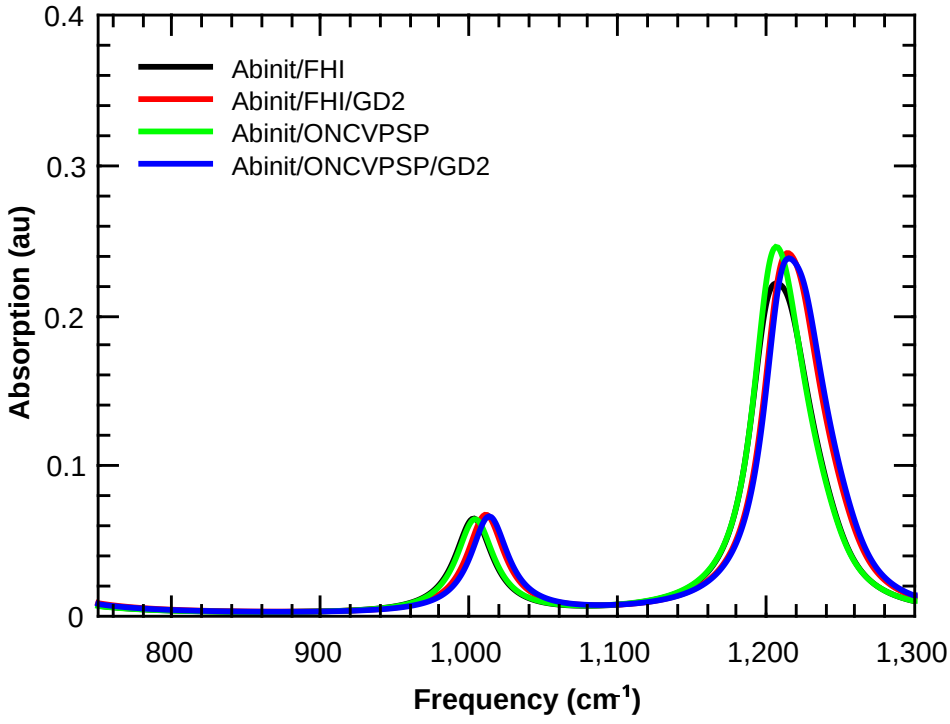

Figure 43: Abinit ATR Spectra - High Frequency Range

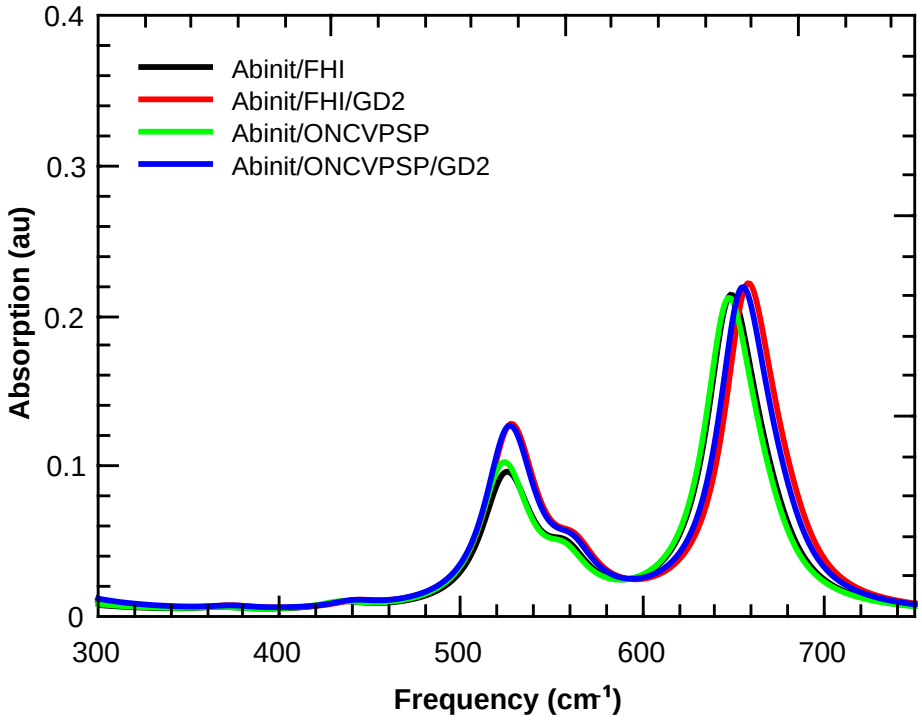

Figure 44: Abinit ATR Spectra - Intermediate Frequency Range

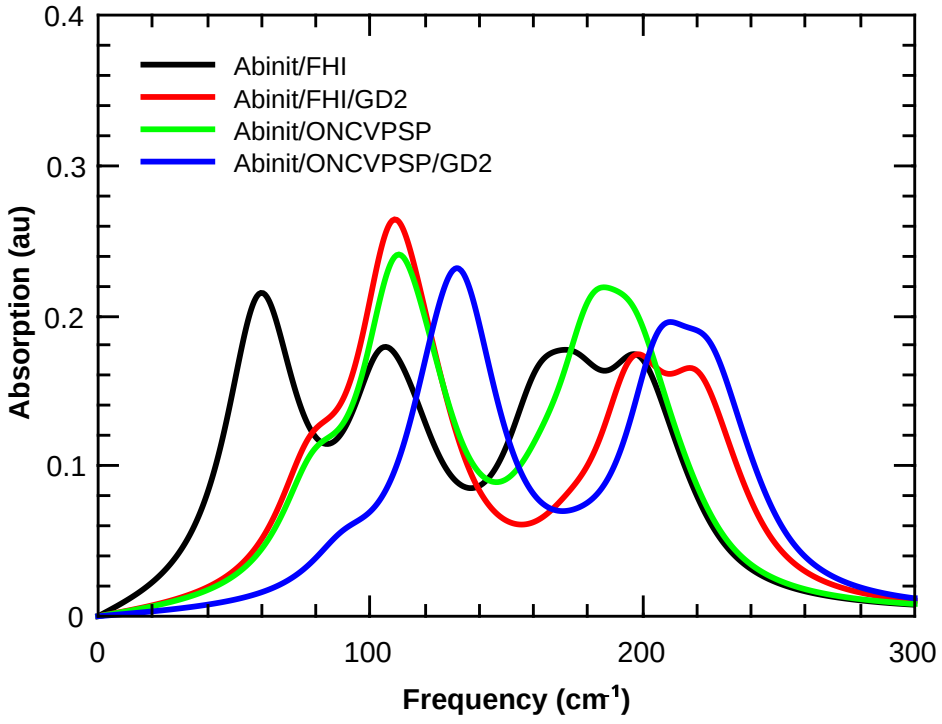

Figure 45: Abinit ATR Spectra - Low Frequency Range

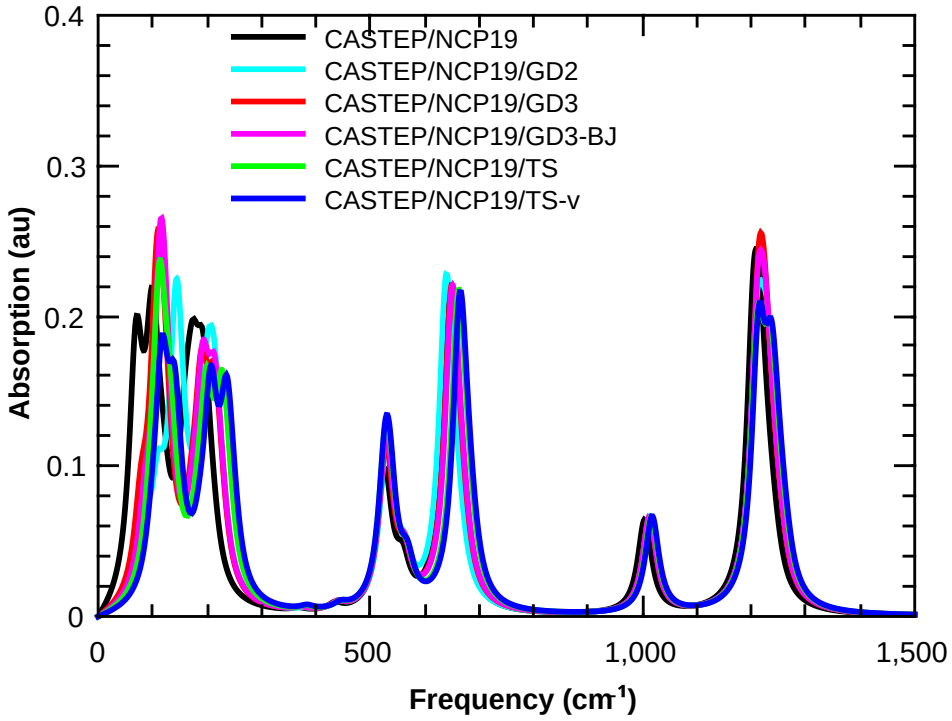

Figure 46: CASTEP ATR Spectra - Full Frequency Range

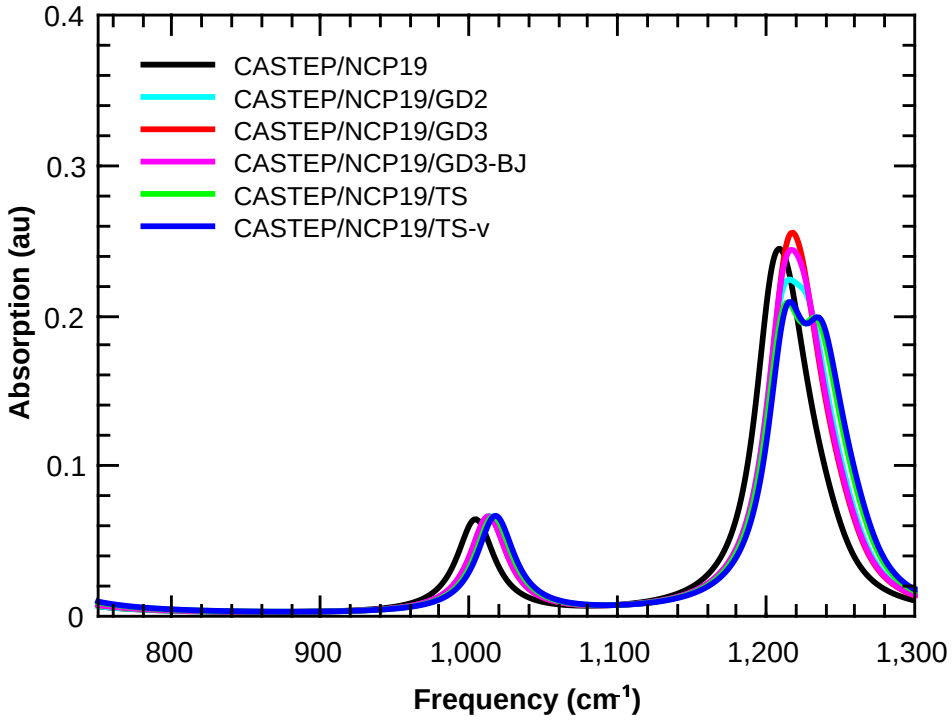

Figure 47: CASTEP ATR Spectra - High Frequency Range

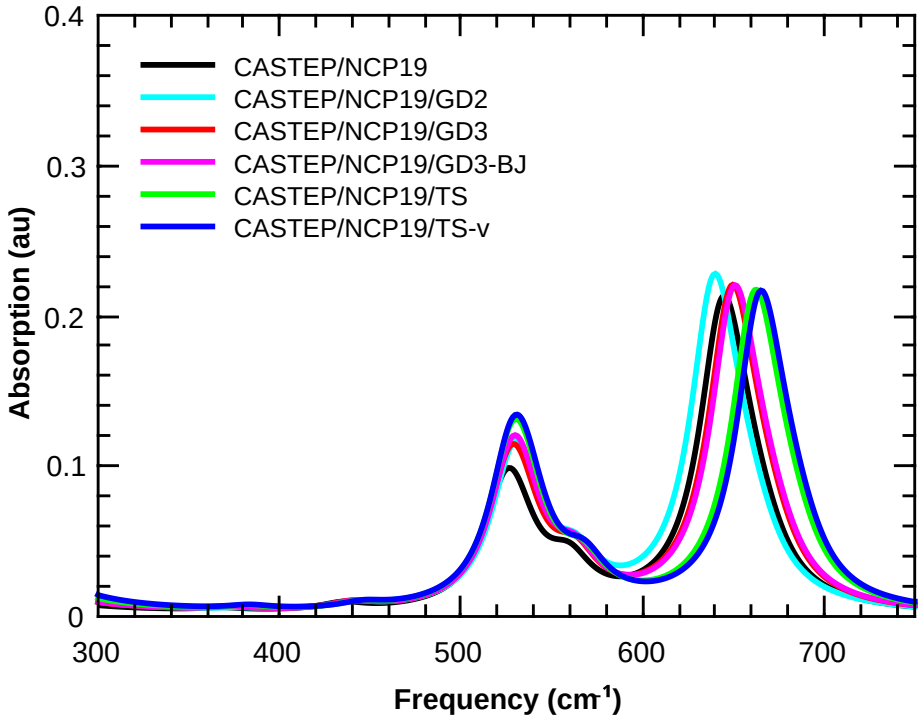

Figure 48: CASTEP ATR Spectra - Intermediate Frequency Range

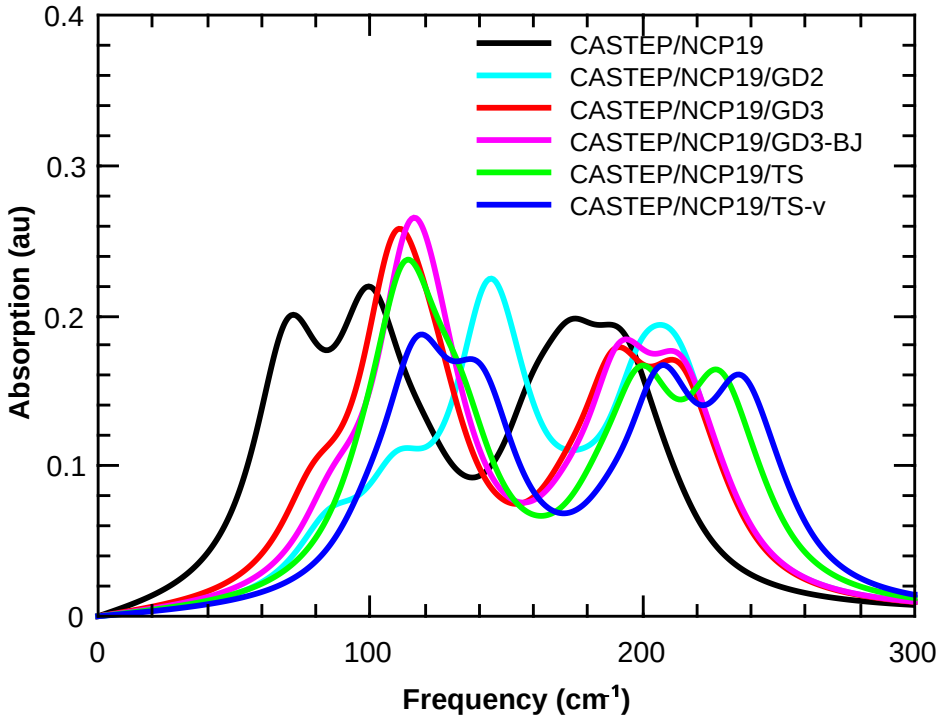

Figure 49: CASTEP ATR Spectra - Low Frequency Range

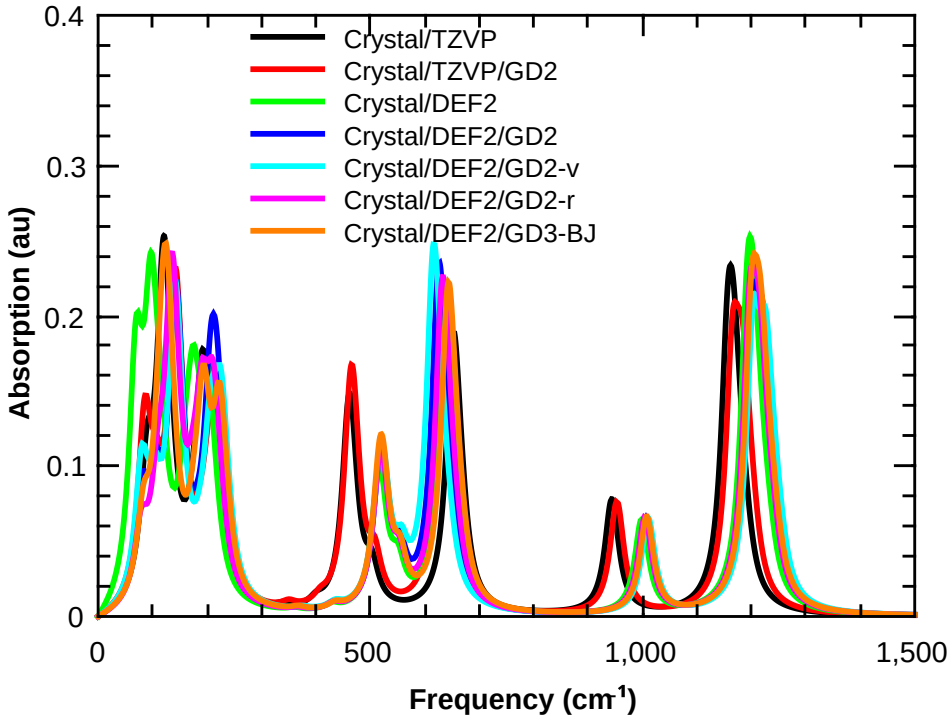

Figure 50: Crystal ATR Spectra - Full Frequency Range

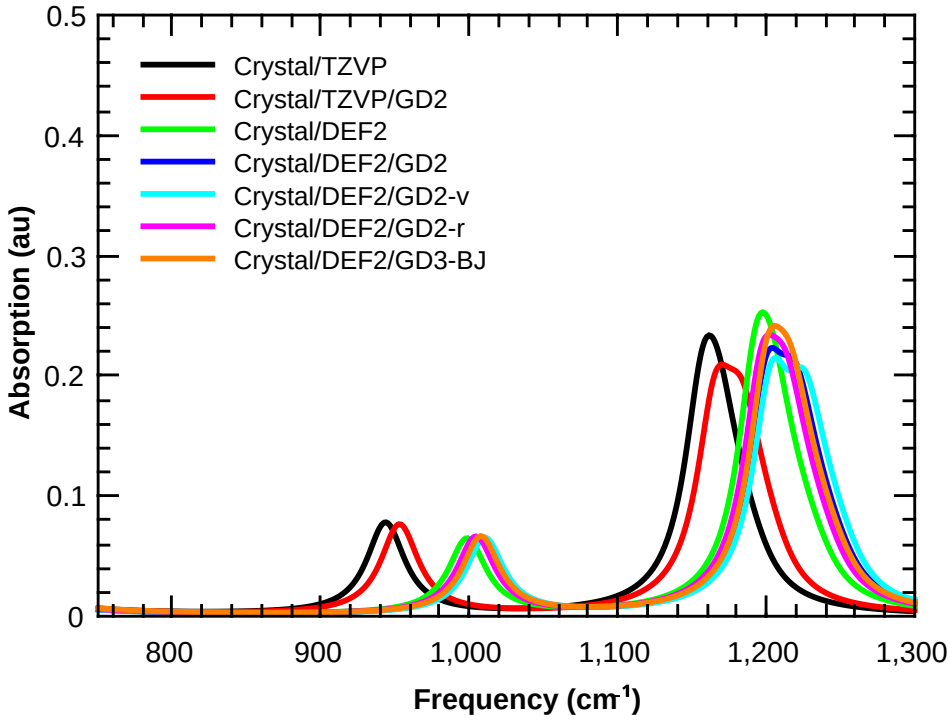

Figure 51: Crystal ATR Spectra - High Frequency Range

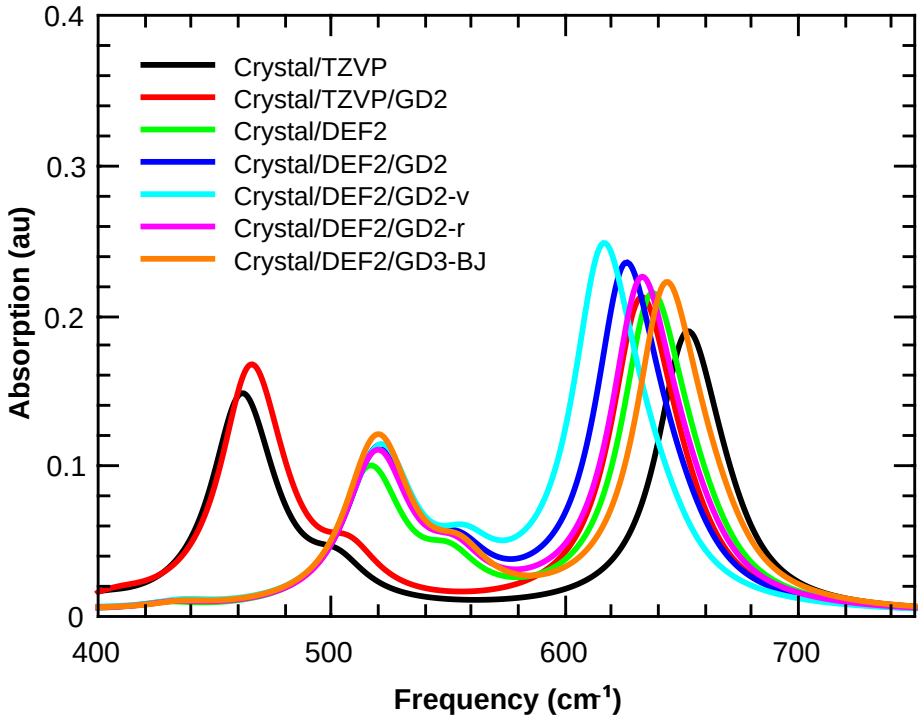

Figure 52: Crystal ATR Spectra - Intermediate Frequency Range

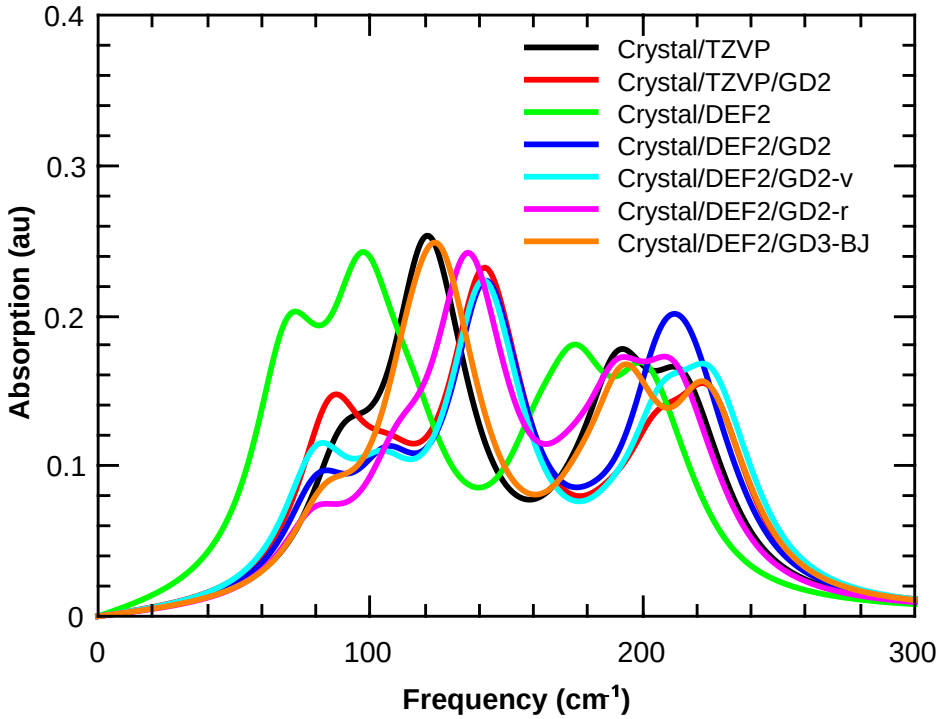

Figure 53: Crystal ATR Spectra - Low Frequency Range

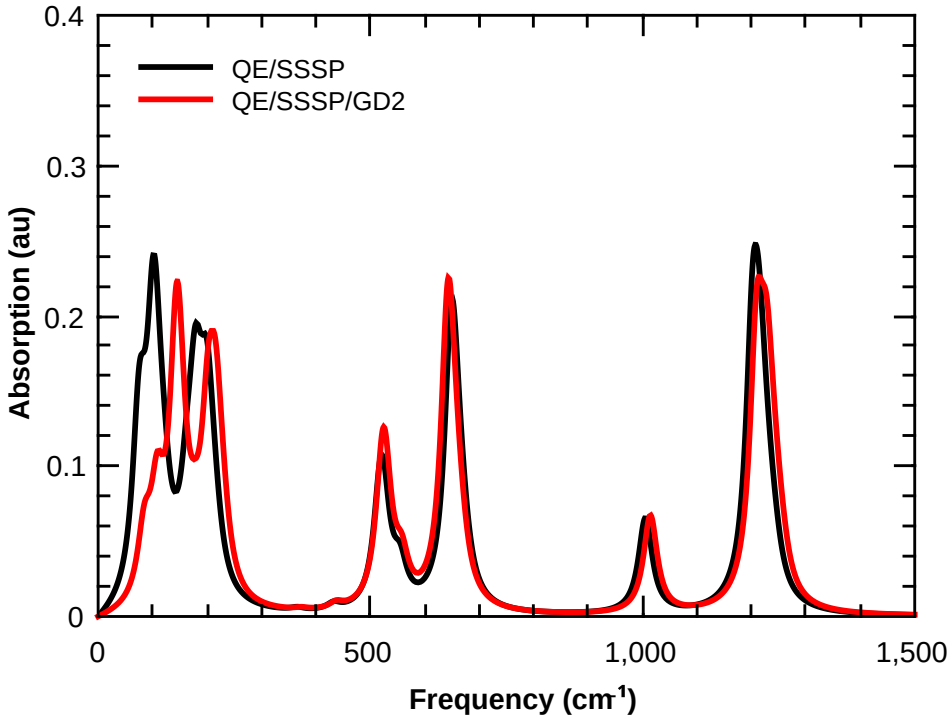

Figure 54: QE ATR Spectra - Full Frequency Range

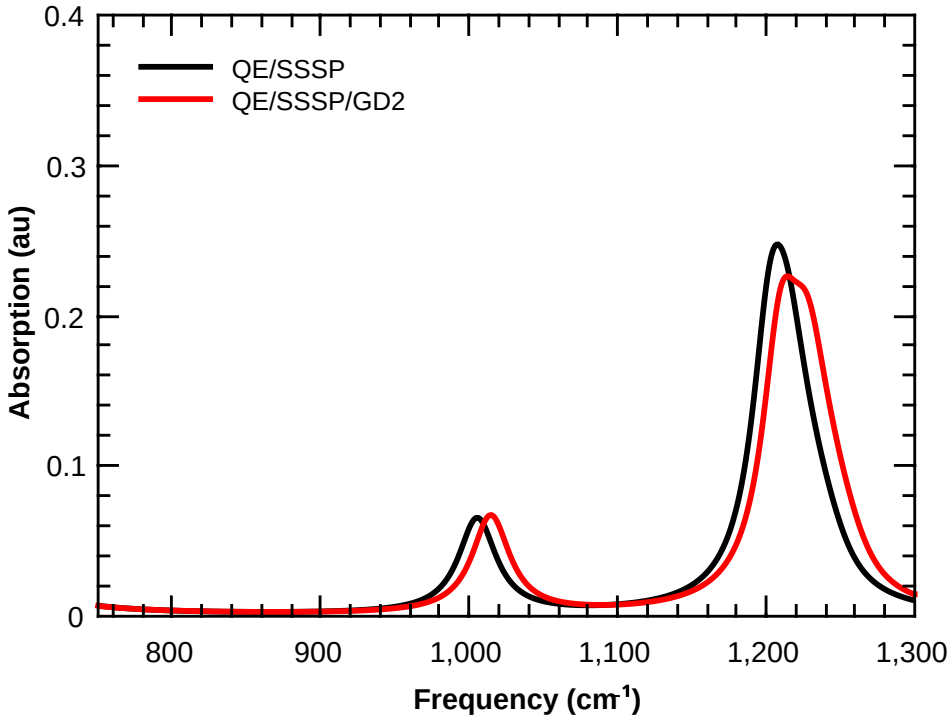

Figure 55: QE ATR Spectra - High Frequency Range

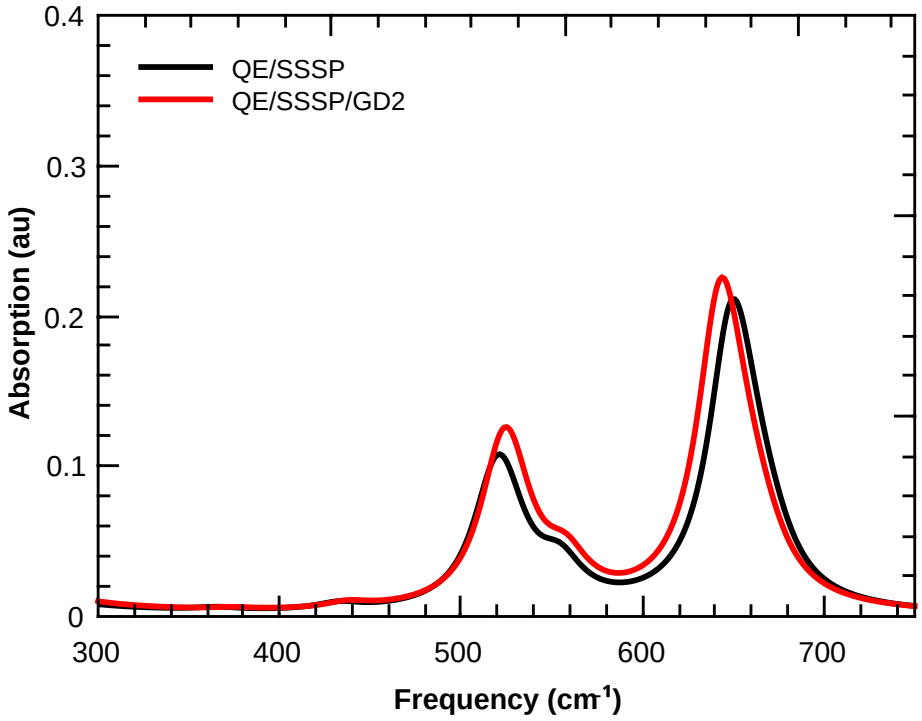

Figure 56: QE ATR Spectra - Intermediate Frequency Range

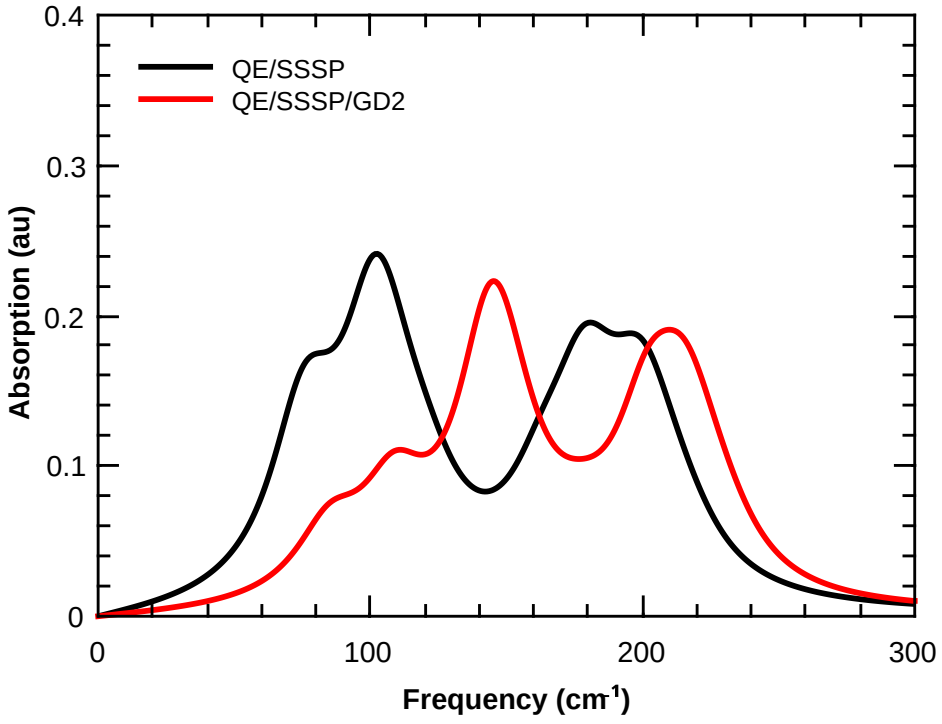

Figure 57: QE ATR Spectra - Low Frequency Range

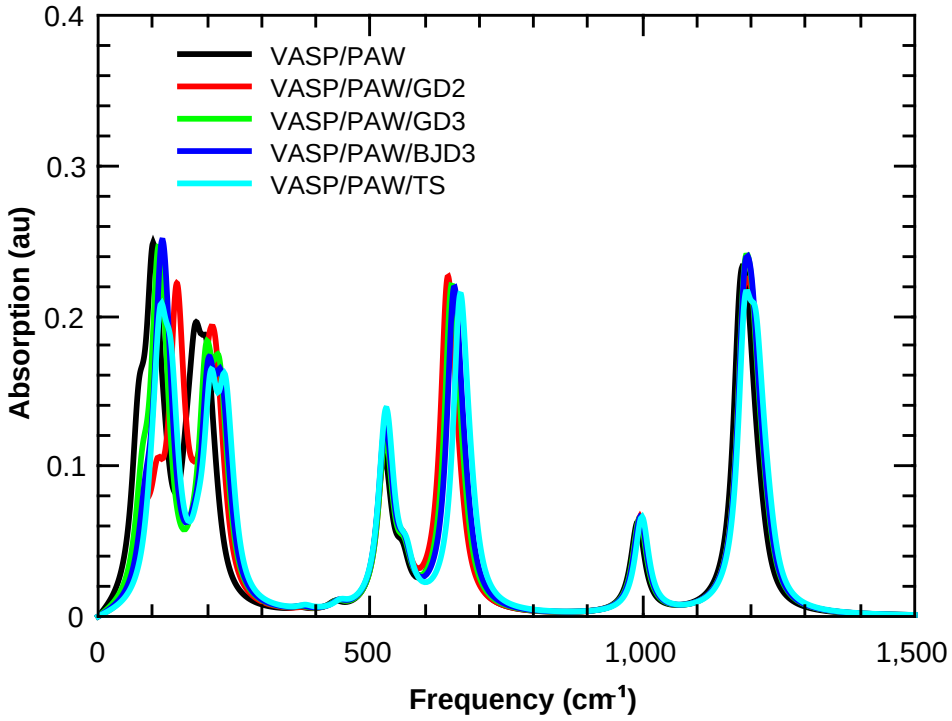

Figure 58: VASP ATR Spectra - Full Frequency Range

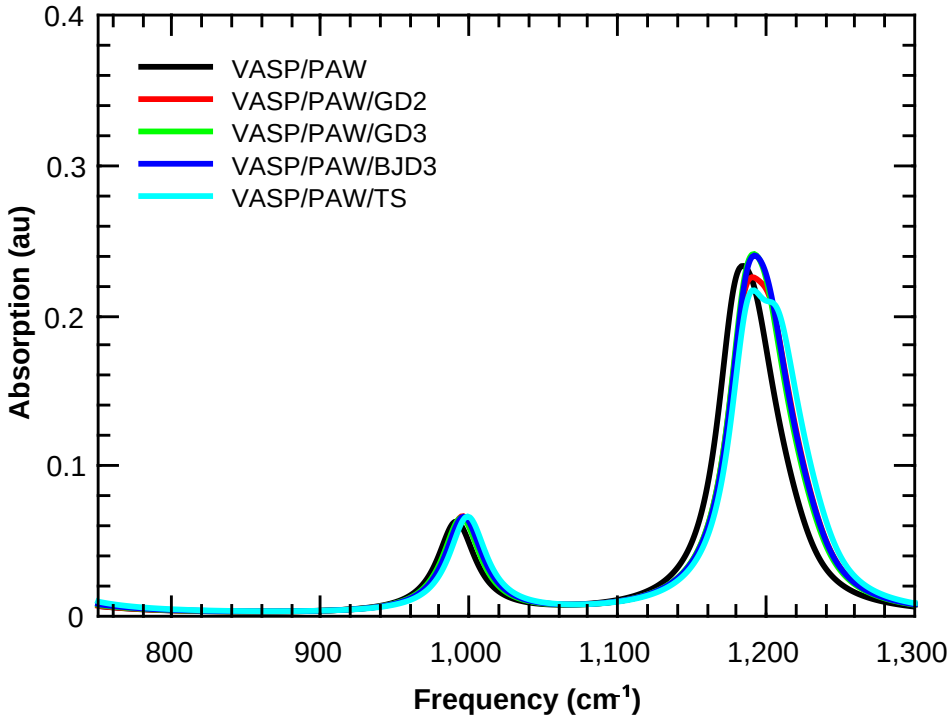

Figure 59: VASP ATR Spectra - High Frequency Range

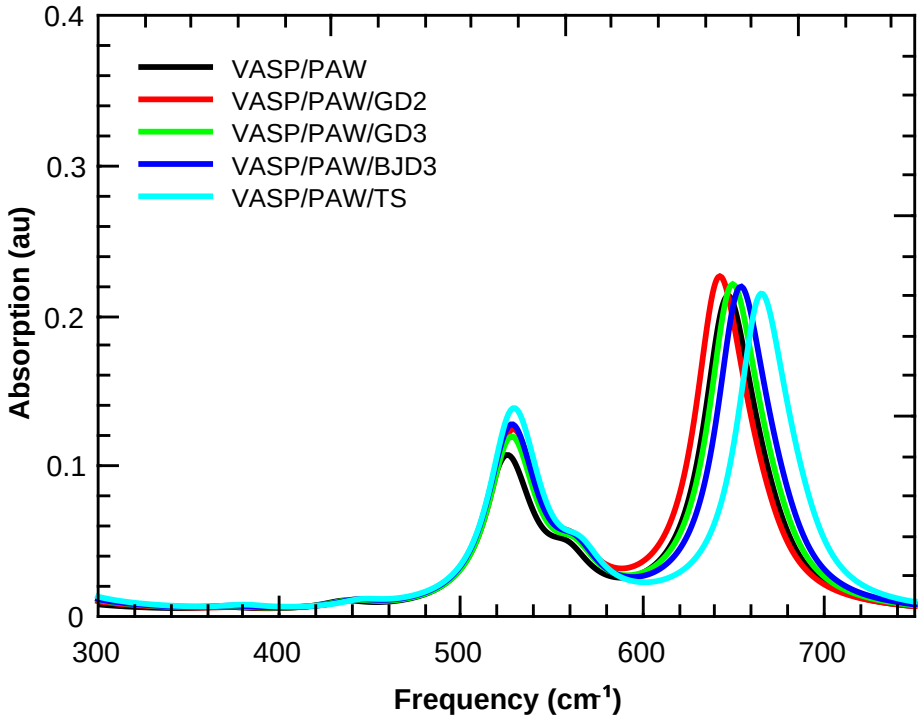

Figure 60: VASP ATR Spectra - Intermediate Frequency Range

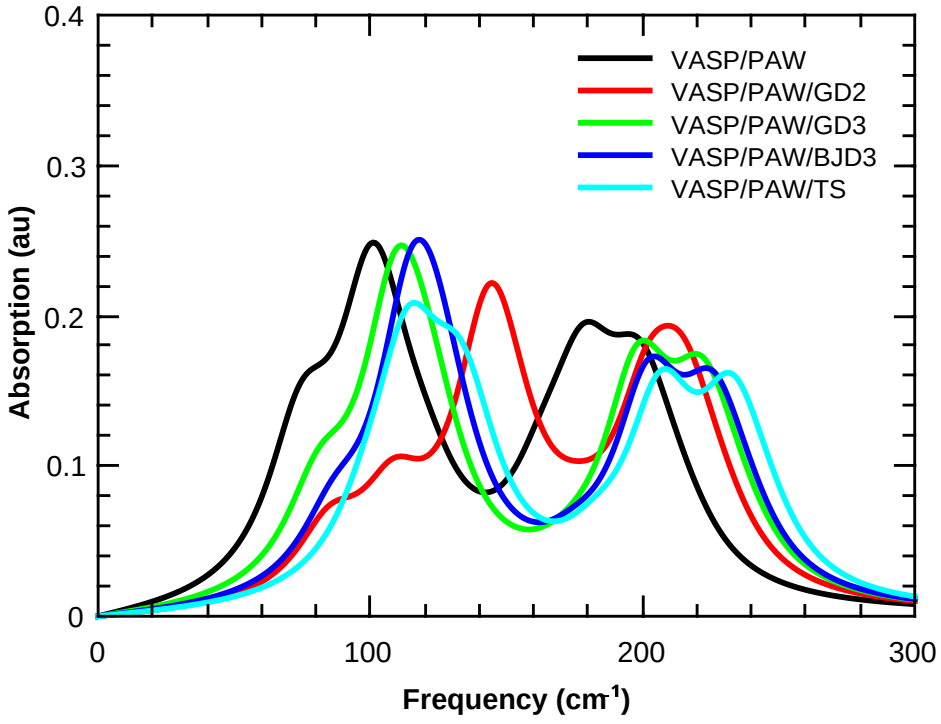

Figure 61: VASP ATR Spectra - Low Frequency Range

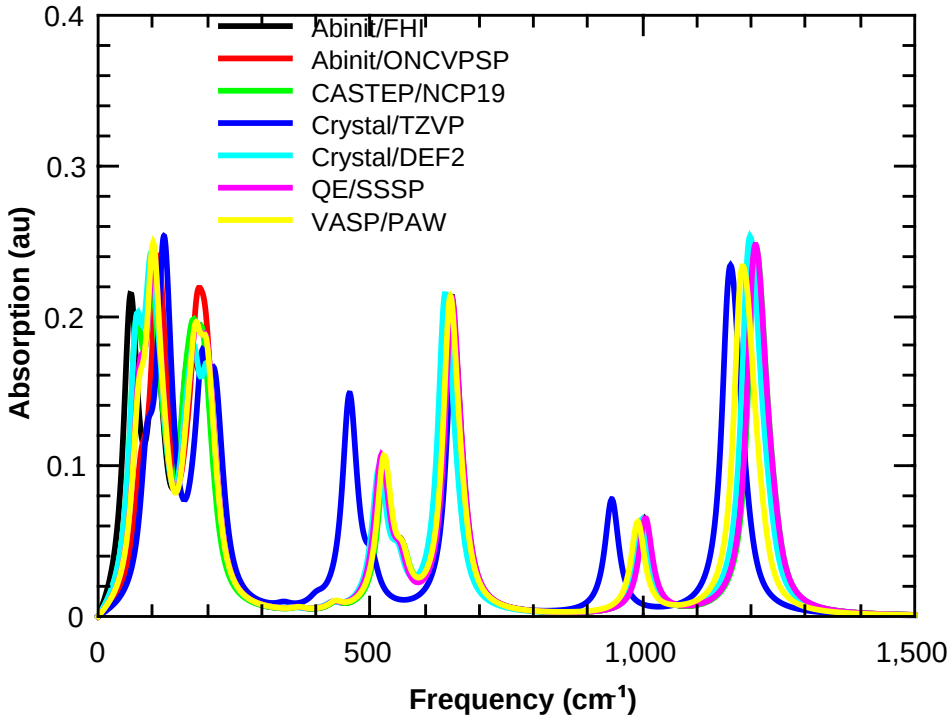

Figure 62: ATR Spectra no dispersion correction, full frequency range

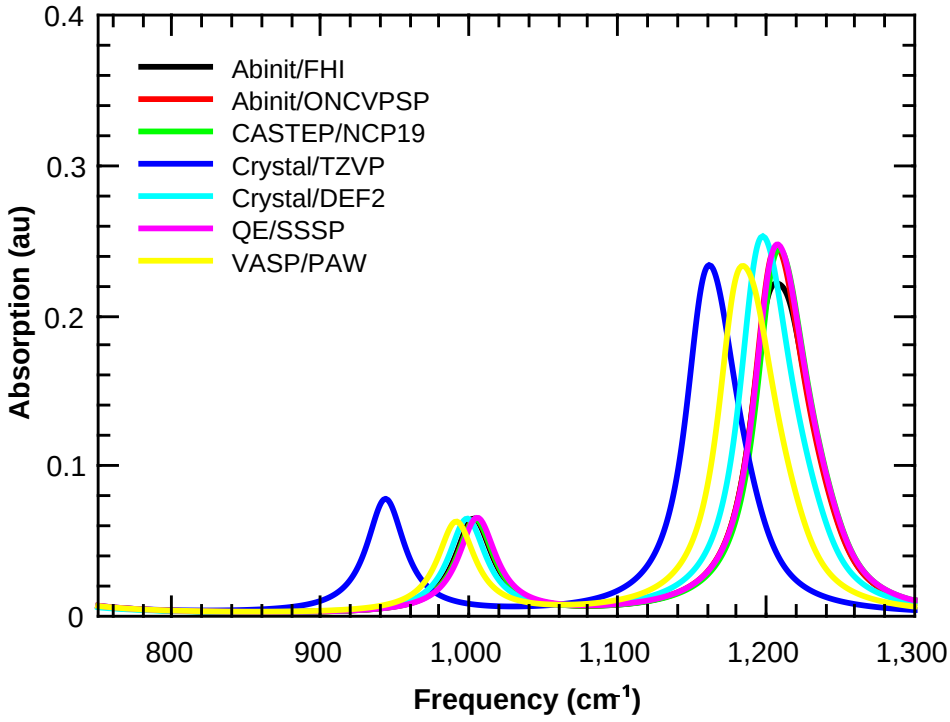

Figure 63: ATR Spectra no dispersion correction, high frequency range

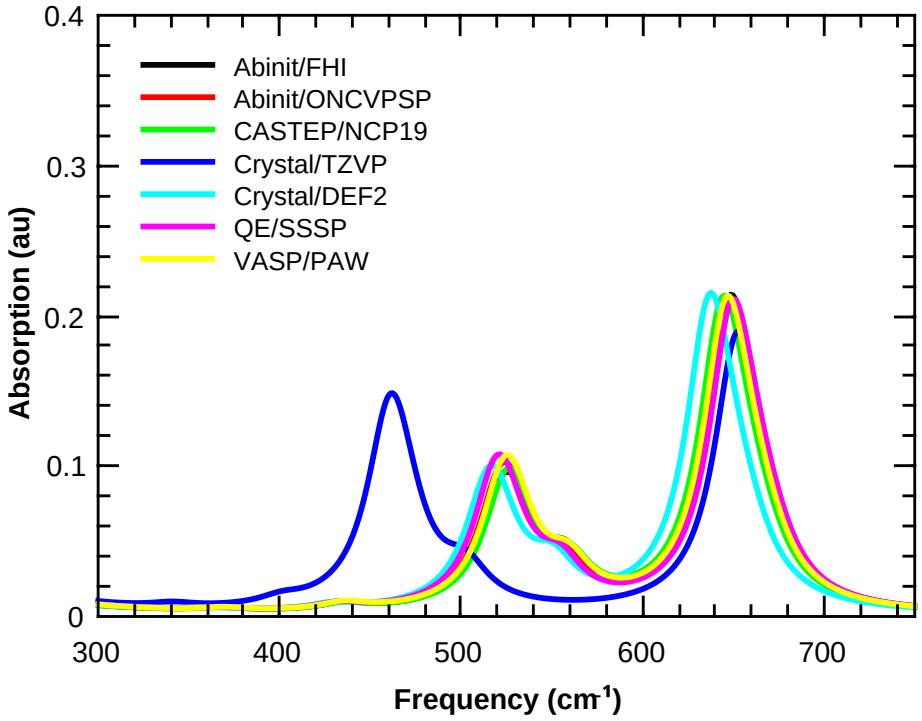

Figure 64: ATR Spectra no dispersion correction, intermediate frequency range

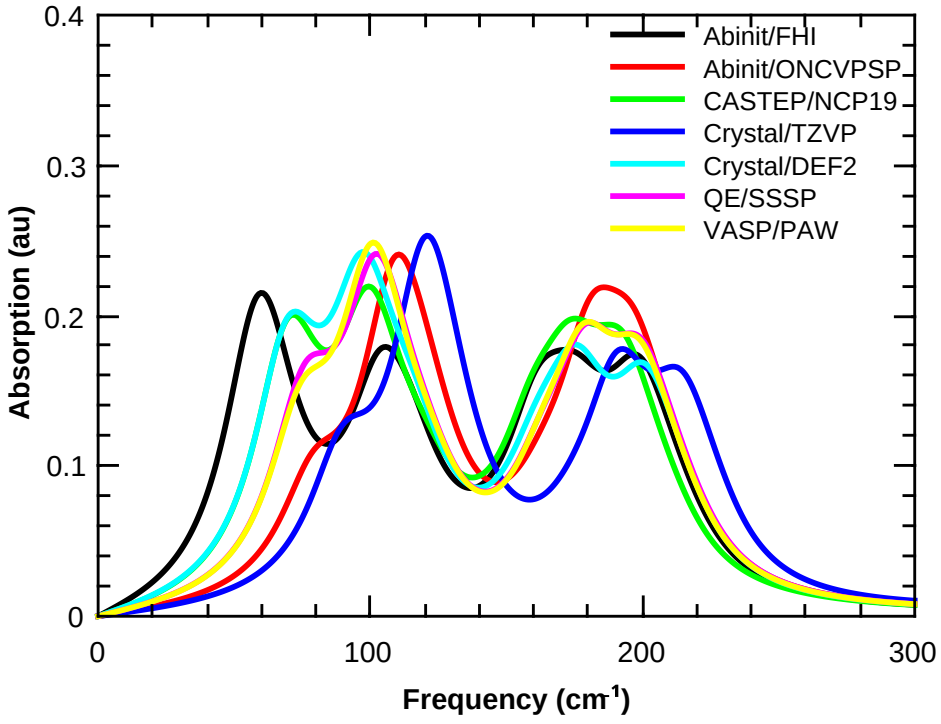

Figure 65: ATR Spectra no dispersion correction, low frequency range

13.1 Comparison of Effective Medium Theories

Figures 66 to 69 compare the ATR absorption spectra calculated using an Averaged Permittivity with the Maxwell-Garnett and Bruggeman effective medium theories at a concentration of 50% volume fraction of sodium peroxodisulfate in air with a Lorentzian width factor of 30 cm^{-1}

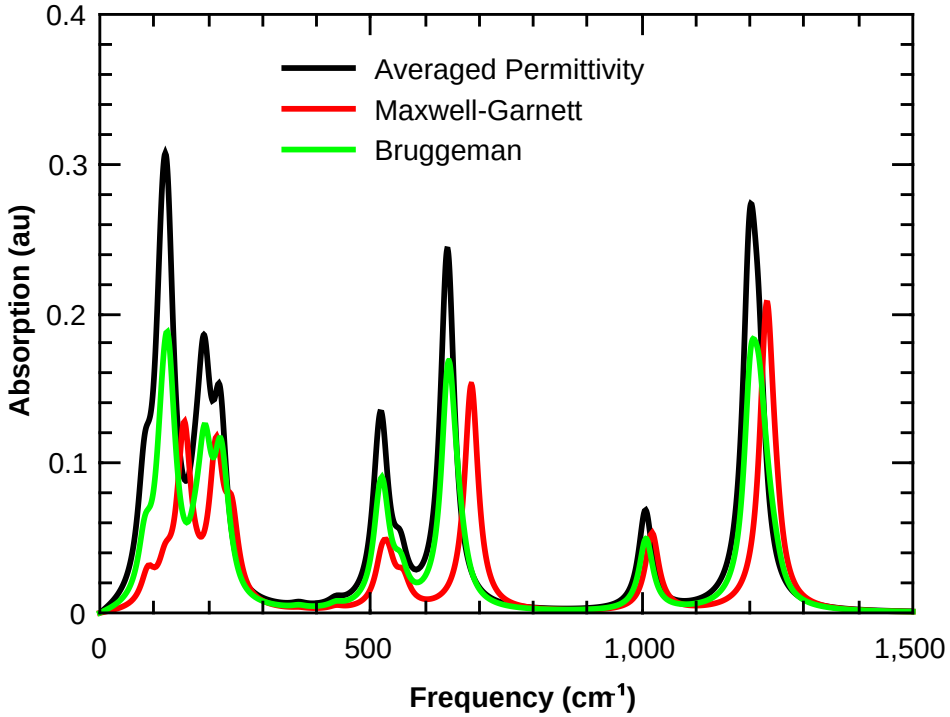

Figure 66: Average Permittivity, Maxwell-Garnett and Bruggeman ATR Absorption from Crystal/DEF2/GD3-BJ, full frequency range

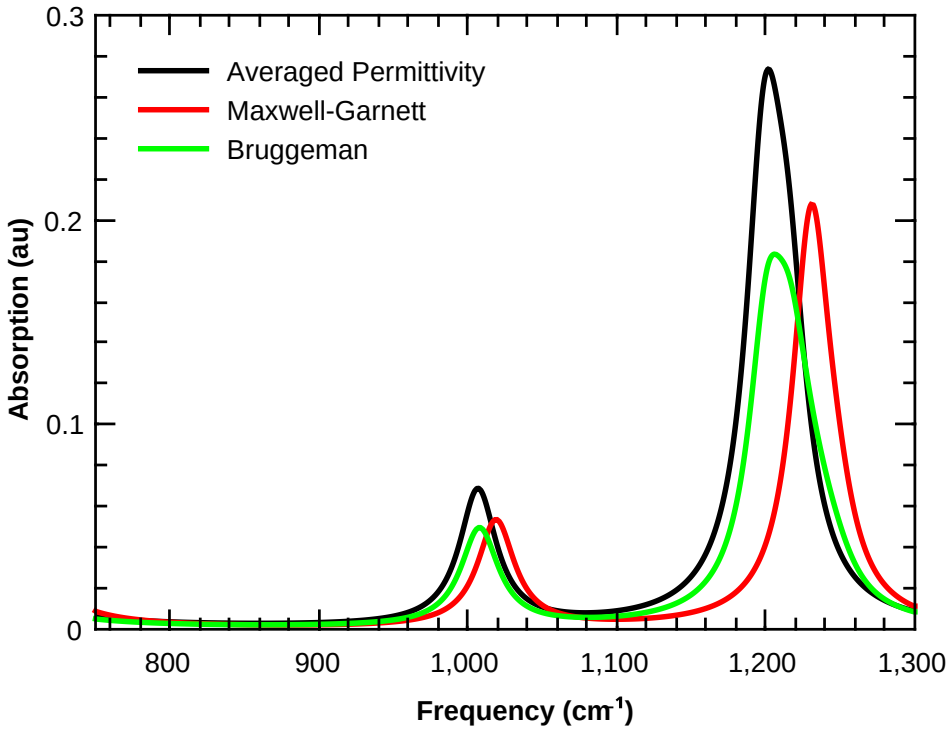

Figure 67: Average Permittivity, Maxwell-Garnett and Bruggeman ATR Absorption from Crystal/DEF2/GD3-BJ, high frequency range

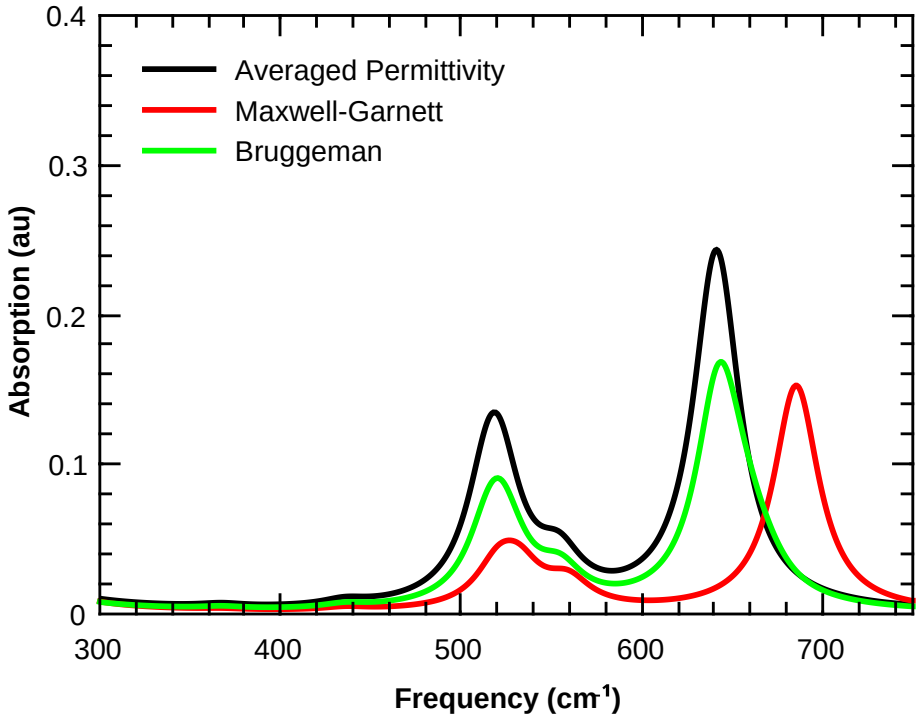

Figure 68: Average Permittivity, Maxwell-Garnett and Bruggeman ATR Absorption from Crystal/DEF2/GD3-BJ, intermediate frequency range

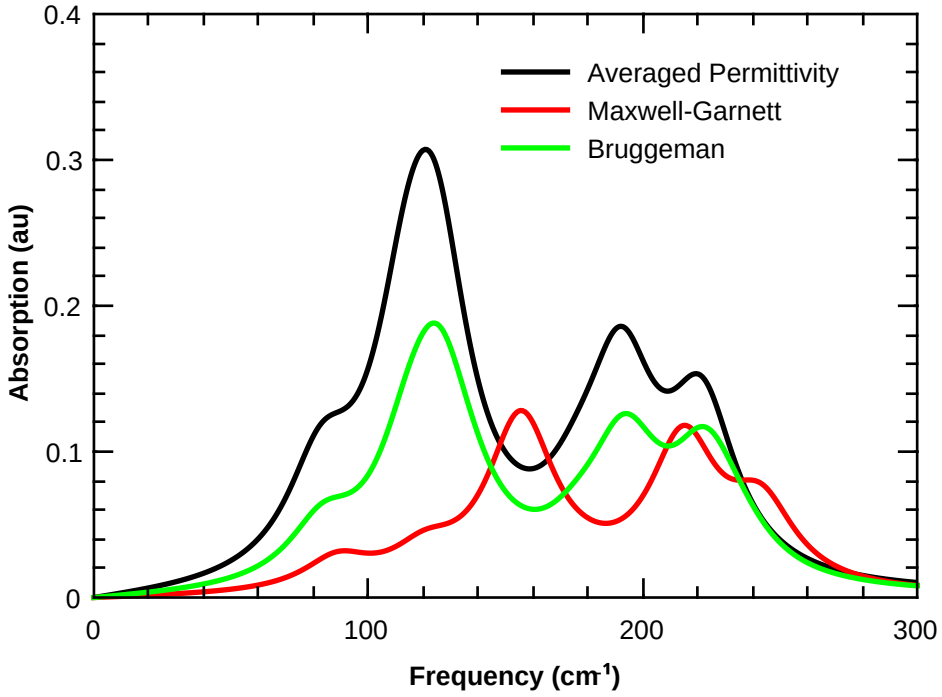

Figure 69: Average Permittivity, Maxwell-Garnett and Bruggeman ATR Absorption from Crystal/DEF2/GD3-BJ, low frequency range

13.2 Comparison of Calculated ATR Spectra

As described in Section 10 above, the calculated spectra can be compared with each other by calculating the normalized cross-correlation coefficient between each pair of spectra which also a 'lag' or frequency shift which maximizes the cross-correlation for each pair of spectra. The cross-correlation matrix is symmetric and the results presented using a gap-map where yellow is used to describe the highest cross-correlation coefficient and blue the lowest with the methods have being clustered according to their similarity. The clustering is made clear by the dendrogram at the top of the heat map. The heat map itself shows the values of the cross-correlation coefficient as a colour map. In Figures 70 to 73 ATR spectra were used in the calculations of the cross-correlation coefficients. The ATR spectra were calculated using an effective permittivity calculated using the Bruggeman method for 50% sodium peroxodisulfate in air with a line broadening factor of $30\,\mathrm{cm}^{-1}$.

Figures 70 and 71 shows a gap-map created using the full frequency range of the spectra while Figures 72 and 73 were created based only the low frequency range of the spectra (below $300\,\mathrm{cm}^{-1}$.

Here the majority of the VASP and CASTEP dispersion corrected calculations are shown to be very similar, to clustering in the top/left of the gap-map with the Crystal/TZVP calculations standing out as being quite different to all the other calculations. The lag frequencies shown in Figure 71 again highlight that the frequency shift which maximizes the correlation between spectra is strongly related to the program used to perform the calculation.

Inspection of Figure 72 from the low frequency spectrum shows some clustering owing to dispersion correction used however Figure 73 shows no obvious pattern as was the case in the Maxwell-Garnett calculations in Section 10.

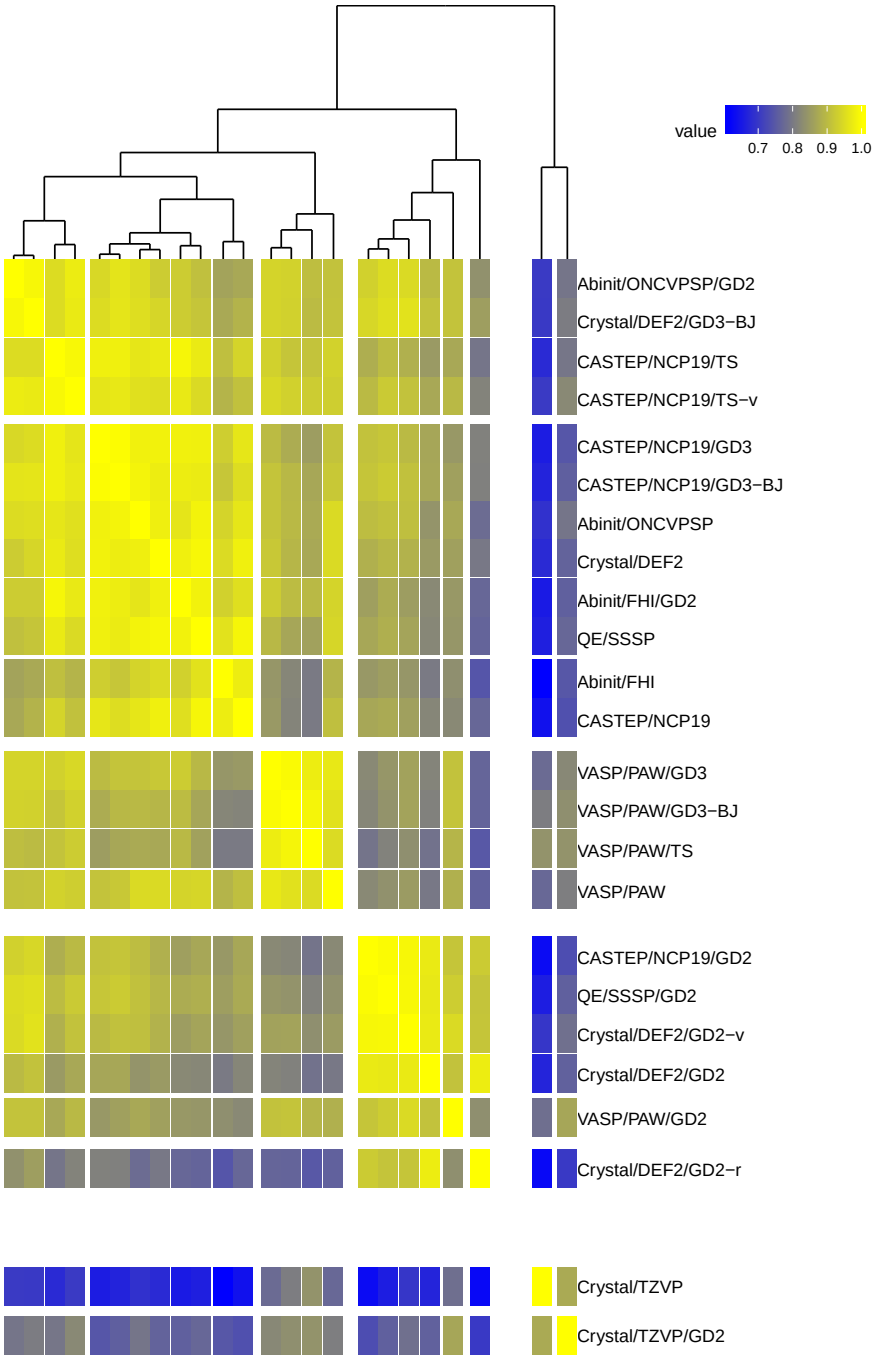

Figure 70: Cross-correlation heat-map of full frequency ATR spectra after clustering

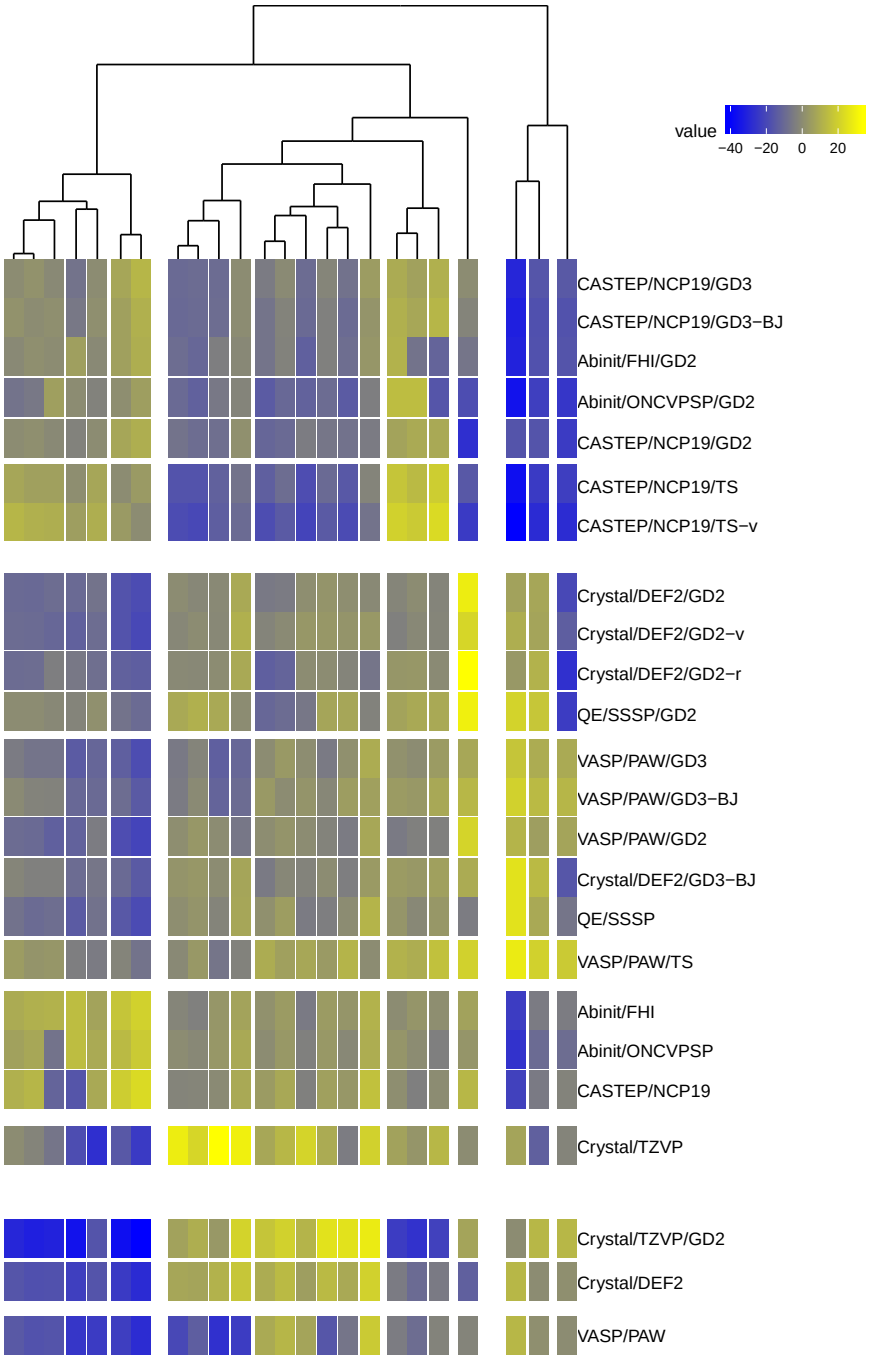

Figure 71: Frequency lag heat-map of full frequency ATR spectra after clustering

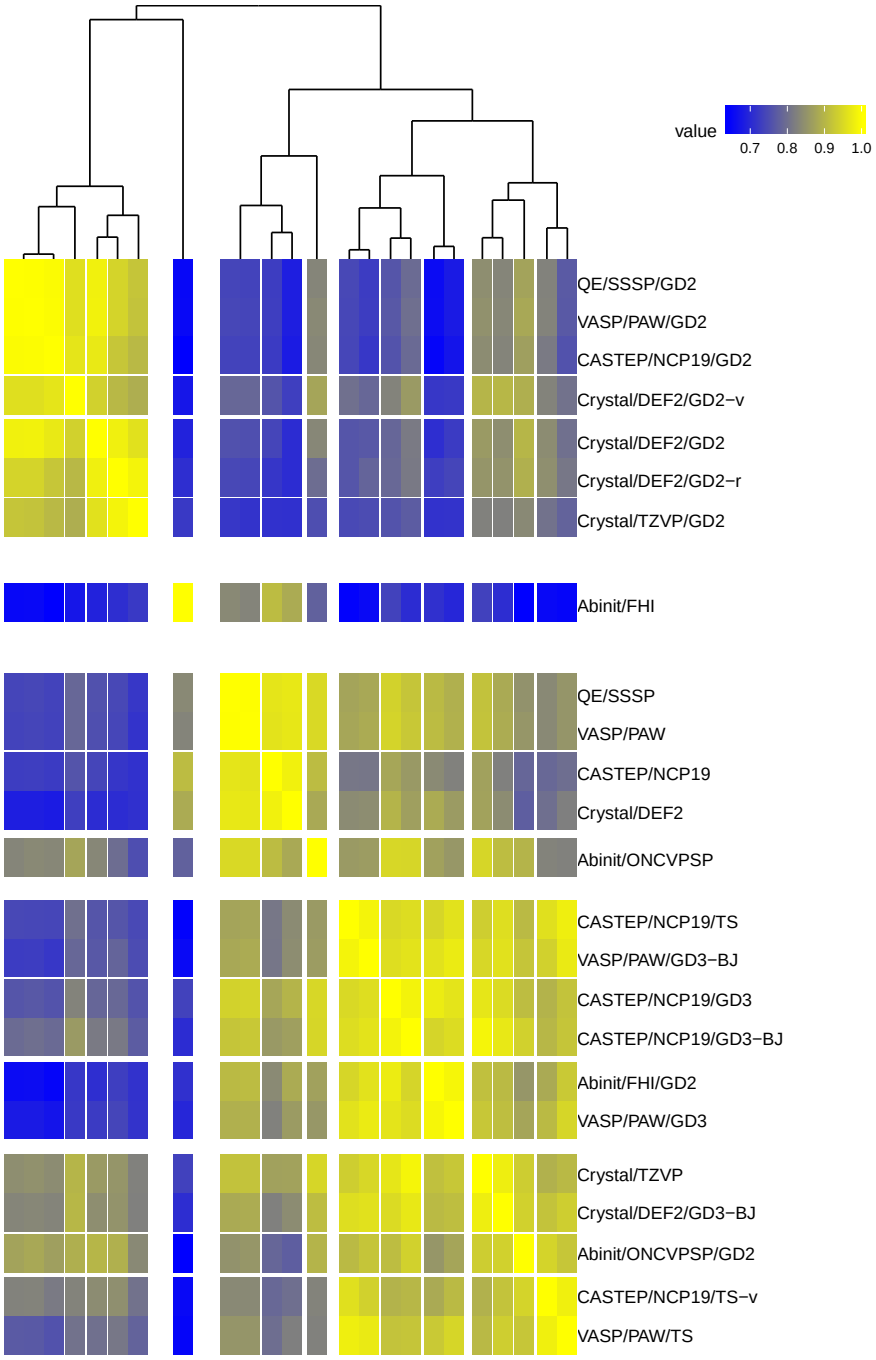

Figure 72: Cross-correlation heat-map of low frequency ATR spectra after clustering

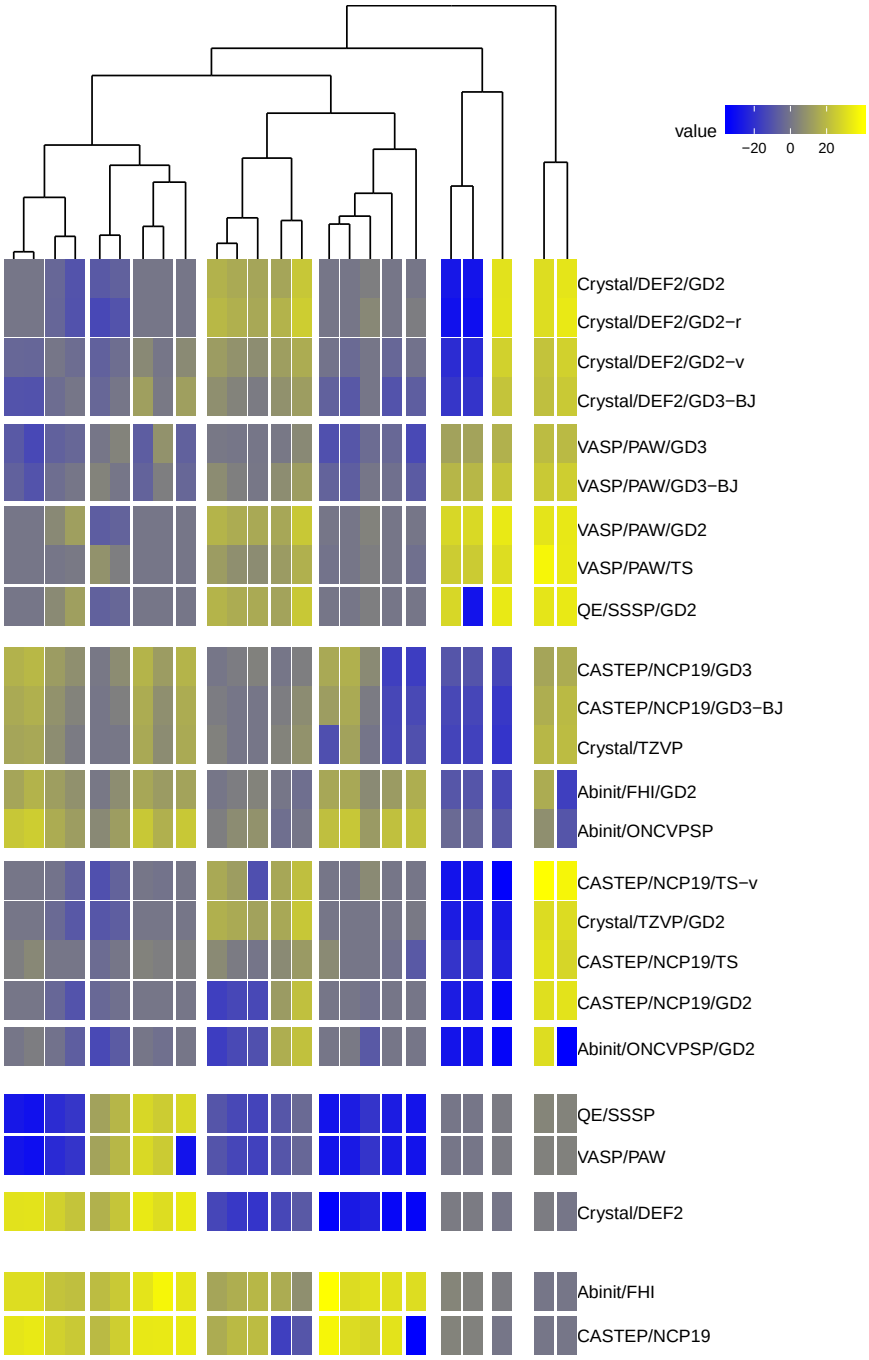

Figure 73: Frequency lag heat-map of low frequency ATR spectra after clustering

13.3 Comparison of Calculated and Experimental ATR Spectra

Table 18 shows the same comparison between the calculated and experimental spectra using a normalized cross-correlation coefficient was calculated between the experimental spectrum in the range 450 to 1400 cm^{-1}.Here the Bruggeman effective medium theory used to calculate the ATR spectrum. In these calculations a 70% volume fraction of $Na_2(SO_4)_2$ was used and the Lorentzian widths adjusted to achieve the same peak heights as the experimental measurements.

To improve the agreement with experiment the frequency of the calculated was re-scaled by a constant factor. Such re-scaling is common in molecular calculations where the systematic errors in the calculated frequency of a particular method are corrected by a scale factor. The reported cross-correlation coefficients in Table 18 are the maximum coefficient at a constant frequency shift. There are therefore two parameters which are optimised to improve the fit with experiment, a frequency shift and a frequency scaling factor. The first three columns in the show the results for the case that no frequency scaling is employed. The last three columns show the results after optimising the frequency scaling factor to improve the cross-correlation coefficient.

Without re-scaling the frequencies, on average the Bruggeman method requires an additional 9.2 cm^{-1} to find the maximum cross-correlation coefficient and the average cross-correlation coefficient is lower the Maxwell-Garnett example by -0.01. However with re-scaling the average cross-correlation coefficient increases by 0.017 compared to Maxwell-Garnett.

Table 18: Scale Factors and cross-correlation coefficients between Bruggeman calculated and experimental ATR spectra

Method	Scale factor	Lag (cm^{-1})	Cross-correlation	Scale factor	Lag (cm^{-1})	Cross-correlation
Abinit/FHI	1	35.4	0.793	1.036	13.2	0.843
Abinit/FHI/GD2	1	31.8	0.846	1.030	12.2	0.880
Abinit/ONCVPSP	1	36.8	0.806	1.034	15.6	0.852
Abinit/ONCVPSP/GD2	1	32.4	0.852	1.025	15.4	0.876
CASTEP/NCP19	1	34.6	0.780	1.045	6.2	0.827
CASTEP/NCP19/GD2	1	30.4	0.781	1.028	11.6	0.810
CASTEP/NCP19/GD3	1	31.0	0.820	1.025	14.5	0.848
CASTEP/NCP19/GD3-BJ	1	30.6	0.819	1.030	10.8	0.851
CASTEP/NCP19/TS	1	28.0	0.862	1.020	14.6	0.884
CASTEP/NCP19/TS-v	1	27.2	0.871	1.016	16.6	0.888
Crystal/TZVP	1	89.2	0.726	1.022	77.4	0.745
Crystal/TZVP/GD2	1	85.4	0.831	1.017	75.6	0.843
Crystal/DEF2	1	44.0	0.801	1.033	23.4	0.851
Crystal/DEF2/GD2	1	39.6	0.784	1.023	23.8	0.806
Crystal/DEF2/GD2-v	1	38.2	0.760	1.020	23.8	0.774
Crystal/DEF2/GD2-r	1	41.2	0.800	1.027	23.6	0.834
Crystal/Def2/GD3-BJ	1	39.6	0.844	1.022	25.0	0.868
QE/SSSP	1	39.0	0.839	1.025	23.0	0.869
QE/SSSP/GD2	1	35.0	0.835	1.016	24.4	0.848
VASP/PAW	1	36.2	0.711	1.063	-0.8	0.866
VASP/PAW/GD2	1	33.6	0.718	1.052	2.0	0.840
VASP/PAW/GD3	1	33.6	0.735	1.056	0.0	0.864
VASP/PAW/GD3-BJ	1	33.2	0.750	1.041	8.0	0.854
VASP/PAW/TS	1	30.6	0.788	1.023	17.0	0.848

14 Experimental Spectra

The experimental infrared and attenuated total reflectance (ATR) spectra are shown in Figure 74.

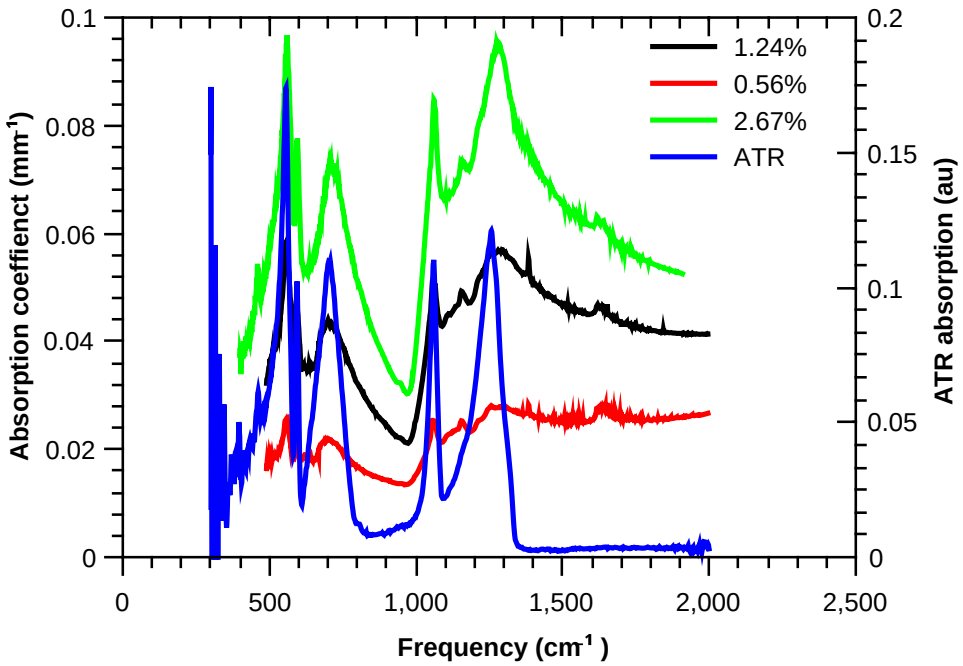

Figure 74: Experimental Infrared Spectra for 0.56%, 1.24% and 2.67% mass fractions and Attenuated Reflectance Spectrum